Orbit Determination for Impulsively Maneuvering Spacecraft using a Modified State Transition Tensor

Xingyu Zhou[1]
Beijing Institute of Technology, Beijing, 100081, China

Malcolm Macdonald[2]
University of Strathclyde, Glasgow, G1 1XJ, UK

and Dong Qiao[3]
Beijing Institute of Technology, Beijing, 100081, China

This paper proposes a method to accurately resolve orbit determination (OD) for a spacecraft with unknown impulsive maneuvers. The proposed method handles the unknown impulsive maneuver by incorporating the magnitude, direction, and time of the impulsive maneuver into the estimation parameter vector. First, a modified state transition tensor (STT) is proposed via orbit division and segment connection, allowing the orbit to be directly propagated under the effects of impulsive maneuver uncertainties. Then, based on the modified STT, a second-order measurement model is established with the estimation parameter vector as the input. Combining the second-order measurement model with observations, a second-order optimal solution is derived to correct the estimation parameters. The spacecraft orbit, together with the magnitude, direction, and time of the impulsive maneuver, are simultaneously estimated in an iterative framework. The performance of the proposed method is validated in a low-Earth-orbit case and a high-Earth-orbit case. Simulations show that the proposed method outperforms its linear version in terms of convergence, accuracy, and uncertainty quantification capacity. Its maneuver reconstruction and orbit estimation errors are one order of magnitude less than those of competitive methods. Moreover, the proposed method can handle severe conditions and is robust to initial guesses.

---

[1] Ph.D. candidate, School of Aerospace Engineering, zhouxingyu@bit.edu.cn
[2] Professor, Department of Electronic and Electrical Engineering, malcolm.macdonald.102@strath.ac.uk (AIAA Associate Fellow)
[3] Professor, School of Aerospace Engineering, qiaodong@bit.edu.cn (Corresponding author)

This is a peer-reviewed, version of record of the following paper: Zhou, X., Macdonald, M., & Qiao, D. (in press). Orbit determination for impulsively maneuvering spacecraft using a modified state transition tensor. Journal of Guidance, Control, and Dynamics.

I. Introduction

ACCURATE tracking, estimation, and prediction of a spacecraft orbit are critically important in all space missions. Several estimators, for example, the least squared method (LSM) and its variants [1], and the Kalman filter (KF) and its variants [2–4], have been widely used in solving the orbit determination (OD) problem. One of the complicated and challenging tasks in OD is to determine and predict the orbit of a maneuvering spacecraft, especially a noncooperative target with unknown maneuvers [5,6]. Without correctly compensating for unknown maneuvers, the OD performance of conventional estimators is significantly degraded, and sometimes these methods even fail to converge [7,8].

The state-of-the-art means of estimating the orbit of a maneuvering spacecraft can be broadly divided into three categories: reinitiation of the OD process, filtering-through approach, and maneuver reconstruction [7]. Reinitiation methods estimate the post-maneuver orbit by directly inflating the estimation covariance [9], disregarding the pre-maneuver measurements and OD solutions. Unknown maneuvers are compensated by the largely inflated initial uncertainty during the state update stage. Reinitiation methods are simple and easy to operate. However, their performance relies on precise maneuver detection and careful selection of the inflating weights. Thus, they are not satisfactory for scenarios with high precision requirements [10].

The filtering-through approach is a real-time tracking technique compensating for unknown maneuvers to fit the post-maneuver observation into the pre-maneuver orbit [7,11]. According to the methods for compensating the unknown maneuver, the filtering-through approach developed thus far can be further cataloged into three groups: the single-model-based adaptive KFs, multiple-model algorithms, and decision-based adaptive KFs [12]. The single-model-based adaptive KFs compensate for the unknown maneuvering accelerations using a single model, including the thrust-Fourier-coefficient (TFC) event representation [7,13,14], the polynomial representation [6] and the variable structure estimator [15]. The multiple-model algorithms use a bank of Kalman filters with different maneuvering submodels in parallel, in which each submodel corresponds to one particular type of maneuver. Typical multiple-model algorithms include the interacting multiple model (IMM) algorithm and its variants [16,17]. The disadvantage of IMM algorithms is that they only work well when the submodels accurately fit the actual maneuvering acceleration. Moreover, the IMM algorithms suffer from algorithm complexity as their computational load increases linearly with the number of submodels [18,19]. The decision-based adaptive KF catalogs include the equivalent noise approaches [20], the input estimation (IE) approaches [21,22], and the switching model (SM)

approaches [23,24]. The equivalent noise approaches and the IE approaches can only be applied to address certain types of maneuvers, and their performances significantly degrade when the actual maneuver varies with time [25]. The SM approaches use nonmaneuvering and maneuvering dynamics and switch according to the maneuver detection results. The SM approaches can perform well but strongly rely on high-frequency observations and accurate maneuver detection [15]. A major concern for the filtering-through approaches is that, although compensating the unknown maneuvers can help improve the estimation accuracy, it is often expected to obtain more information about the maneuver to better track the target, that is, to reconstruct the maneuver [26,27].

Maneuver reconstruction methods are unified by their characterization in postprocessing. There are many ways to reconstruct the unknown maneuver, but all are based on independent estimations of the pre- and post-maneuver orbits [27–29]. The weakness of such methods is that they are sensitive to the estimation errors of the pre- and post-maneuver orbits [29]. In all current maneuver reconstruction methods, the reconstruction process is independent of the orbit estimation. Orbit estimation errors are inevitable due to the measurement noise and the scarce knowledge of the maneuver. In turn, the orbit estimation errors couple and amplify into the errors of the maneuver reconstruction solutions [27,30]. In particular, it is found that the maneuver time is most likely to be distorted by position uncertainties [27]. Moreover, compared with the first two categories, the maneuver reconstruction method usually has heavy computational overhead [7].

The abovementioned methods are mainly developed for ideal OD scenarios, assuming all data preprocessing is done. There is also some literature that contributes to solving more difficult and complex versions of maneuvering spacecraft OD problems. Holzinger *et al*. proposed an optimal control-based estimation (OCBE) method for multi-maneuvering target tracking [31,32]. The OCBE uses a control effort as a defined metric to correlate target observations, detect maneuvers, and characterize maneuvers before estimating the orbit. Hall and Singla developed a unified reachability-based framework for tracking lost-in-space noncooperative maneuvering targets [33,34]. Their method uses numerical quadrature methods to efficiently propagate the reachability sets of the maneuvering target [35,36], which can be further employed for searching lost-in-space targets and tasking sensors, maneuver detection and estimation, and orbit estimation [37].

The method presented in this paper falls into the maneuver reconstruction category. The key difficulty of the impulsively maneuvering spacecraft OD lies in accurately estimating the vector and the time of the unknown impulsive maneuver. One single unknown impulsive maneuver is assumed to occur to simplify the problem. The

proposed method incorporates the vector and the time of the unknown impulsive maneuver into the estimation parameter vector when modeling the OD system. It can estimate the orbits and reconstruct the impulsive maneuver simultaneously. As such, the effects of the orbit estimation errors on the maneuver reconstruction are reduced, while the accuracy and robustness of the maneuver reconstruction method are improved. This paper first models the effects of the impulsive maneuver vector and epoch on the orbits from the view of uncertainty propagation. Under the effects of the impulsive maneuver, the orbit of the spacecraft is divided into several segments. A virtual state is defined to handle the time uncertainty of the impulsive maneuver. Based on the original state transition tensor (STT) technique, a modified second-order STT is proposed for the orbit propagation considering impulsive maneuver uncertainties via virtual state reversion and segment connection. Then, based on the modified STT, a second-order measurement model is proposed to establish the mapping relationship from the estimation parameter vector to the measurements. Starting from the given a priori parameter estimation, the reference orbit is propagated using the modified STT, and the residuals between incoming observation data and predicted measurements are calculated. Based on the partials provided by the second-order measurement model, the concept of the second-order optimal estimation is extended from the conventional least-squares solution. The correction to the a priori parameter estimation is made from the second-order optimal estimation. The impulsively maneuvering spacecraft OD problem is solved in an iterative framework, and thus, the algorithm efficiency is greatly improved.

The remainder of this paper is organized as follows. Section II describes the impulsively maneuvering spacecraft OD problem. Section III addresses the impulsively maneuvering spacecraft OD problem using the modified STT technique. The second-order measurement model and the second-order optimal estimation solution are presented in detail. In Section IV, numerical simulations are performed to investigate the performance of the proposed algorithm. Finally, conclusions are given in Sec. V.

II. Preliminaries

A. Description of an impulsively maneuvering spacecraft OD problem

Consider an OD problem in which the target executes one unknown impulsive maneuver. Assume that the orbit state of the target is labeled as $\boldsymbol{x}=[\boldsymbol{r};\boldsymbol{v}]$, where $\boldsymbol{r}=[x,y,z]^T$ and $\boldsymbol{v}=[\dot{x},\dot{y},\dot{z}]^T$ denote the position and velocity vectors in the Earth-centered equatorial inertial (ECEI) coordinate system, respectively. The OD process begins at epoch t_0 and ends at epoch t_2. An impulsive maneuver $\Delta\boldsymbol{v}_1=[\Delta v_x;\Delta v_y;\Delta v_z]$ is applied at epoch t_1, where

$t_1 \in (t_0, t_2)$. The conventional OD process only estimates the orbit of the spacecraft. In this paper, we aim to estimate the orbit, and the time and vector of the impulsive maneuver together. Thus, the estimation parameter vector $\boldsymbol{X}$ is written as

$$\boldsymbol{X} = [\boldsymbol{r}; \boldsymbol{v}; \Delta\boldsymbol{v}_1; t_1]. \tag{1}$$

The system equation of the impulsively maneuvering spacecraft OD problem is given by

$$\begin{cases} \dot{\boldsymbol{x}} = \boldsymbol{y}(\boldsymbol{x}, t) \in \mathbb{R}^6 \\ \boldsymbol{z} = \boldsymbol{h}(\boldsymbol{x}) + \boldsymbol{\varepsilon} \in \mathbb{R}^d \end{cases}, \tag{2}$$

where $\boldsymbol{y}(\boldsymbol{x}, t) \in \mathbb{R}^6$ represents the state model, $\boldsymbol{h}(\boldsymbol{x}) \in \mathbb{R}^d$ is the measurement model, d is the dimension of the measurement vector, and $\boldsymbol{\varepsilon} \in \mathbb{R}^d$ is the Gaussian-distributed measurement noise with the covariance matrix represented by $\boldsymbol{R} \in \mathbb{R}^{d \times d}$.

Finally, the point mass gravity of Earth and the Earth's oblateness perturbation J_2 are expressed as

$$\begin{cases} \dot{\boldsymbol{r}} = \boldsymbol{v} \\ \dot{\boldsymbol{v}} = -\dfrac{\mu_e}{\|\boldsymbol{r}\|^3}\boldsymbol{r} + \boldsymbol{a}_{J_2}(\boldsymbol{r}) \end{cases}, \tag{3}$$

where $\mu_e = 398600.44 \text{ km}^3/\text{s}^2$ is the gravitational constant of the Earth, and $\boldsymbol{a}_{J_2}(\boldsymbol{r})$ is the perturbation acceleration of J_2, given by

$$\boldsymbol{a}_{J_2}(\boldsymbol{r}) = \begin{bmatrix} \mu_e x J_2 \dfrac{R_e^2}{\|\boldsymbol{r}\|^5}\left(-\dfrac{3}{2} + \dfrac{15}{2}\dfrac{z^2}{\|\boldsymbol{r}\|^2}\right) \\ \mu_e y J_2 \dfrac{R_e^2}{\|\boldsymbol{r}\|^5}\left(-\dfrac{3}{2} + \dfrac{15}{2}\dfrac{z^2}{\|\boldsymbol{r}\|^2}\right) \\ \mu_e z J_2 \dfrac{R_e^2}{\|\boldsymbol{r}\|^5}\left(-\dfrac{9}{2} + \dfrac{15}{2}\dfrac{z^2}{\|\boldsymbol{r}\|^2}\right) \end{bmatrix}, \tag{4}$$

where $R_e = 6378.137 \text{ km}$ denotes the Earth's radius, and $J_2 = 1.08264 \times 10^{-3}$.

B. State transition tensor technique

The STT technique is a classic analytical nonlinear propagation method derived from the higher-order Taylor series approach [38–41]. Let $\boldsymbol{x}_0$ and $\boldsymbol{x}(t)$ denote the state at the initial epoch t_0 and an arbitrary future epoch t,

respectively. From Eq. (2), the deviation of the state $\boldsymbol{x}$ from a reference (nominal) orbit can be approximated by the *N*-th order Taylor series expansion at the initial state $\boldsymbol{x}_0$ as:

$$\delta x^i(t) = \sum_{p=1}^{N} \frac{1}{p!} \Phi_{(t_0,t)}^{i,k_1\cdots k_p} \delta x_0^{k_1} \cdots \delta x_0^{k_p} \ , \tag{5}$$

where $x^i(t)$ ($i \in \{1,2,3,4,5,6\}$) denotes the *i*-th elements of the state vector $\boldsymbol{x}(t)$, $x_0^{k_j}$ ($k_j \in \{1,2,3,4,5,6\}$) is the k_j-th component of the state vector $\boldsymbol{x}_0$, and $\Phi_{(t_0,t)}^{i,k_1\cdots k_p}$ is the *p*-th order STT from t_0 to t, given by

$$\Phi_{(t_0,t)}^{i,k_1\cdots k_p} = \frac{\partial^p x^i(t)}{\partial x_0^{k_1} \cdots \partial x_0^{k_p}} . \tag{6}$$

Note that in Eqs. (5) and (6) (and the equations in the following parts of this paper), the Einstein summation notation is used for all the dummy variables (*i.e.*, k_1, k_2, …, k_p) [42,43]. For example, for the second-order term $\Phi_{(t_0,t)}^{i,k_1k_2} \delta x_0^{k_1} \delta x_0^{k_2}$, the subscripts k_1 and k_2 traverse from 1 to 6 in the summation, such that

$$\Phi_{(t_0,t)}^{i,k_1k_2} \delta x_0^{k_1} \delta x_0^{k_2} = \sum_{k_1=1}^{6} \sum_{k_2=1}^{6} \Phi_{(t_0,t)}^{i,k_1k_2} \delta x_0^{k_1} \delta x_0^{k_2} \ . \tag{7}$$

The STTs $\Phi_{(t_0,t)}^{i,k_1\cdots k_p}$ can be obtained by integrating the differential equations. The differential equations for obtaining the STTs (up to second-order) are expressed as

$$\dot{\Phi}_{(t_0,t)}^{i,k_1} = y_{\text{ref}}^{i,p_1} \Phi_{(t_0,t)}^{p_1,k_1} , \tag{8}$$

$$\dot{\Phi}_{(t_0,t)}^{i,k_1k_2} = y_{\text{ref}}^{i,p_1} \Phi_{(t_0,t)}^{p_1,k_1k_2} + y_{\text{ref}}^{i,p_1p_2} \Phi_{(t_0,t)}^{p_1,k_1} \Phi_{(t_0,t)}^{p_2,k_2} , \tag{9}$$

where p_1 and p_2 are dummy variables used for summation convention; $y_{\text{ref}}^{i,k_1\cdots k_p}$ is the partials of the dynamic equation $\boldsymbol{y}(\boldsymbol{x},t)$ computed along the reference orbit $\boldsymbol{x}_{\text{ref}}$, given by

$$y_{\text{ref}}^{i,k_1\cdots k_p} = \left. \frac{\partial^p y^i(\boldsymbol{x},t)}{\partial x^{k_1} \cdots \partial x^{k_p}} \right|_{\boldsymbol{x}=\boldsymbol{x}_{\text{ref}}} . \tag{10}$$

III. Methodology

This section divides the proposed method of solving the impulsively maneuvering spacecraft OD problem into three parts. First, the modified STT for orbit propagation is proposed, considering the impulsive maneuver vector and epoch uncertainty. Then the second-order measurement model is derived based on the modified STT. The second-order optimal estimation is proposed by combining the second-order measurement model and the incoming

observations, and a multiple-iterative solving framework is presented. Finally, the overall procedures of the proposed methodology are summarized.

A. Modified state transition tensor considering impulsive maneuver uncertainty

Assume that the target executes one unknown impulsive maneuver during $[t_0, t_2]$. The impulsively maneuvering spacecraft OD problem is shown in Fig. 1. The states of the real orbit and the reference orbit are labeled by $\tilde{\boldsymbol{x}}(t)$ and $\boldsymbol{x}(t)$, respectively. The blue lines represent the reference state ($\boldsymbol{x}_0 = \boldsymbol{x}(t_0)$, $\boldsymbol{x}_1^-$, $\boldsymbol{x}_1^+$ and $\boldsymbol{x}_2 = \boldsymbol{x}(t_2)$), while the red lines represent the real state ($\tilde{\boldsymbol{x}}_0 = \tilde{\boldsymbol{x}}(t_0)$, $\tilde{\boldsymbol{x}}_1^-$, $\tilde{\boldsymbol{x}}_1^+$ and $\tilde{\boldsymbol{x}}_2 = \tilde{\boldsymbol{x}}(t_2)$). The green state ($\boldsymbol{x}_1^*$) is named the virtual state, which is used as an intermediate variable to assist the formula derivation in this paper.

As shown in Fig. 1 (a) and (b), the definitions of the virtual state $\boldsymbol{x}_1^*$ are different in the cases of $\delta t_1 < 0$ and $\delta t_1 \geq 0$. For the case of $\delta t_1 < 0$, the virtual state is defined as the state of $\tilde{\boldsymbol{x}}(t)$ at epoch t_1 (see Fig. 1(a)). For the case of $\delta t_1 \geq 0$, $\boldsymbol{x}_1^*$ is the state obtained by propagating $\tilde{\boldsymbol{x}}_1^+$ back from epoch $\tilde{t}_1$ to t_1 (see Fig. 1(b)). Note that for the two considered cases, the proposed modified STTs are the same. The reference state can be propagated according to the current estimations in an LSM or a KF process. $\boldsymbol{x}_0$ and $\boldsymbol{x}_2$ are the state at the beginning epoch and the final epoch in the OD process, respectively. $\boldsymbol{x}_1^-$ and $\boldsymbol{x}_1^+$ are the states before and after the instance of the impulsive maneuver. $\Delta\boldsymbol{x}_1 = \boldsymbol{x}_1^+ - \boldsymbol{x}_1^- = [\boldsymbol{0}_{3\times1}; \Delta\boldsymbol{v}_1]$ is the impulsive maneuver. $\delta\boldsymbol{x}_0$, $\delta\boldsymbol{x}_1^-$, $\delta\boldsymbol{x}_1^+$, $\delta\Delta\boldsymbol{x}_1 = [\boldsymbol{0}_{3\times1}; \delta\Delta\boldsymbol{v}_1]$, $\delta\boldsymbol{x}_2$ and δt_1 are the deviation states.

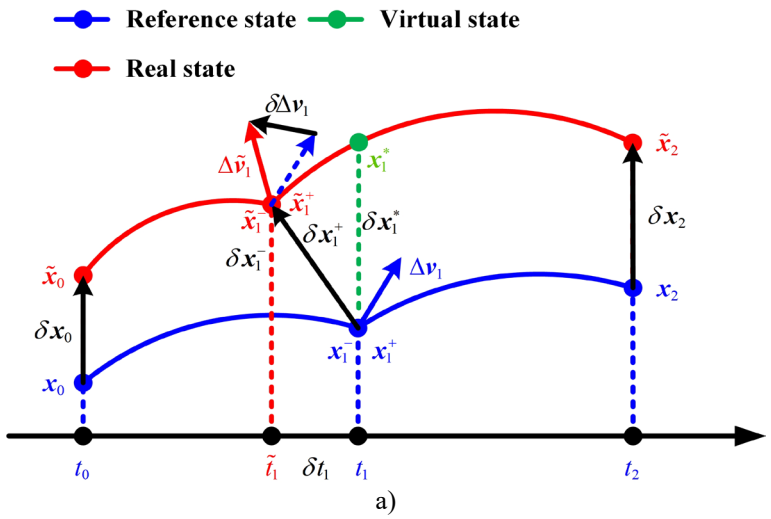

a)

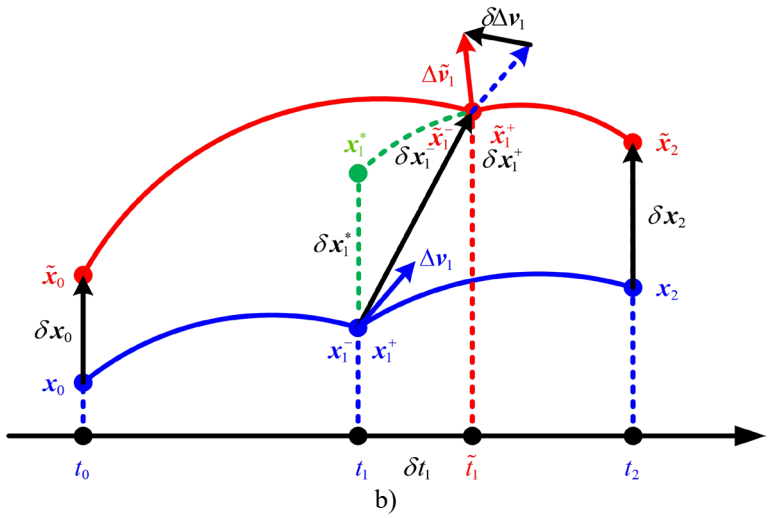

Fig. 1 A description of the variables in an impulsive OD problem. a) Case of $\delta t_1 < 0$. b) Case of $\delta t_1 \geq 0$.

Assuming that the dynamics are accurate, the orbit during $[t_0, t_2]$ can be fully determined by $\boldsymbol{x}_0$, t_1 and $\Delta\boldsymbol{x}_1$ ($\Delta\boldsymbol{v}_1$). With the current estimations $\boldsymbol{x}_0$, t_1 and $\Delta\boldsymbol{v}_1$ obtained, the goal of the impulsive OD is to determine the deviations $\delta\boldsymbol{x}_0$, $\delta\Delta\boldsymbol{x}_1 = [\boldsymbol{0}_{3\times1}; \delta\Delta\boldsymbol{v}_1]$ and δt_1 .

The modified STT is used to analytically model the relationship between the deviation $\delta\boldsymbol{x}(t)$ $(t_0 \leq t \leq t_2)$ and the deviations $\delta\boldsymbol{x}_0$, $\delta\Delta\boldsymbol{x}_1$ and δt_1 . According to the definitions of epochs t_0 , t_1 , $\tilde{t}_1$ and t_2 , in this paper, the orbit of the impulsively maneuvering spacecraft during $[t_0, t_2]$ is divided into three segments. The first orbit segment begins from the epoch t_0 and ends at the epoch $\tilde{t}_1$. The second segment is between epochs $\tilde{t}_1$ and t_1 . The third segment is in $[t_1, t_2]$. The modified STT is proposed by connecting these segments.

Consider the first segment. In the period $t_0 \leq t \leq t_1$, the deviation state $\delta\boldsymbol{x}(t)$ can be represented by a second-order expression as

$$\delta x^k(t) = \Phi^{k,p}_{(t_0,t)} \delta x_0^p + \frac{1}{2} \Psi^{k,p_1p_2}_{(t_0,t)} \delta x_0^{p_1} \delta x_0^{p_2} , \tag{11}$$

where $\Phi^{k,p}_{(t_0,t)}$ and $\Psi^{k,p_1p_2}_{(t_0,t)}$ are the first-order STT and second-order STT of the dynamics in Eq. (3), $\delta x^k(t)$ is the k-th element of the $\delta\boldsymbol{x}(t)$, and δx_0^p is the p-th element of $\delta\boldsymbol{x}_0$. We use the second-order expression in this study because the second-order STTs can adequately capture the nonlinearity of the Earth-centered dynamics [42,44].

Substituting $t = t_1$ into Eq. (11), we have

$$\delta x^k(t_1) = \Phi^{k,p}_{(t_0,t_1)}\delta x_0^p + \frac{1}{2}\Psi^{k,p_1p_2}_{(t_0,t_1)}\delta x_0^{p_1}\delta x_0^{p_2}\,. \tag{12}$$

Then, taking the influence of δt_1 into consideration, the second-order solution to the deviation state $\delta \boldsymbol{x}_1^-$ is expressed as

$$\begin{aligned}\delta x_1^{-,k} &= \delta x^k(t_1) + f_-^k\delta t_1 + \frac{1}{2}g_-^k\delta t_1\delta t_1 + H_-^{k,p}\delta t_1\delta \boldsymbol{x}_0^p \\ &= \Phi^{k,p}_{(t_0,t_1)}\delta x_0^p + \frac{1}{2}\Psi^{k,p_1p_2}_{(t_0,t_1)}\delta x_0^{p_1}\delta x_0^{p_2} + f_-^k\delta t_1 + \frac{1}{2}g_-^k\delta t_1\delta t_1 + H_-^{k,p}\delta t_1\delta \boldsymbol{x}_0^p\end{aligned}, \tag{13}$$

where $\delta x_1^{-,k}$ is the k-th component of the state vector $\delta \boldsymbol{x}_1^-$, and

$$f_-^k = \frac{\partial x_1^{-,k}}{\partial t_1} = y^k(\boldsymbol{x}_1^-, t_1)\,, \tag{14}$$

$$g_-^k = \frac{\partial^2 x_1^{-,k}}{\partial t_1\partial t_1} = \frac{\partial y^k(\boldsymbol{x}_1^-, t_1)}{\partial t_1}, \tag{15}$$

$$H_-^{k,p} = \frac{\partial^2 x_1^{-,k}}{\partial t_1\partial \boldsymbol{x}_0^p} = \frac{\partial}{\partial t_1}\left(\frac{\partial x_1^{-,k}}{\partial \boldsymbol{x}_0^p}\right) = \frac{\partial[\Phi^{k,p}_{(t_0,t_1)}(\boldsymbol{x}_1^-)]}{\partial t_1} = \dot{\Phi}^{k,p}_{(t_0,t_1)}(\boldsymbol{x}_1^-) = \frac{\partial y^k(\boldsymbol{x}_1^-, t_1)}{\partial x_1^{-,p}}. \tag{16}$$

Equations (13)-(16) are the proposed second-order propagators of the first segment.

Now, we investigate the propagation in the second segment. By adding the deviation of the impulsive maneuver $\delta\Delta \boldsymbol{x}_1$ into Eq. (13), the deviation state $\delta \boldsymbol{x}_1^+$ is expressed as

$$\delta x_1^{+,k} = \delta x_1^{-,k} + \delta\Delta x_1^k\,. \tag{17}$$

According to the definition of the virtual state $\boldsymbol{x}_1^*$, the relationship between $\delta \boldsymbol{x}_1^*$ and $\delta \boldsymbol{x}_1^+$ can be found by performing a Taylor series expansion in terms of the state $\boldsymbol{x}_1^+$, given by

$$\delta x_1^{+,k} = \delta x_1^{*,k} + f_+^k\delta t_1 + \frac{1}{2}g_+^k\delta t_1\delta t_1 + H_+^{k,p}\delta t_1\delta x_1^{*,p} = \delta x_1^{-,k} + \delta\Delta x_1^k\,, \tag{18}$$

where

$$f_+^k = \frac{\partial x_1^{+,k}}{\partial t_1} = y^k(\boldsymbol{x}_1^+, t_1)\,, \tag{19}$$

$$g_+^k = \frac{\partial^2 x_1^{+,k}}{\partial t_1\partial t_1} = \frac{\partial y^k(\boldsymbol{x}_1^+, t_1)}{\partial t_1}, \tag{20}$$

$$H_+^{k,p} = \frac{\partial^2 x_1^{+,k}}{\partial t_1\partial x_1^{+,p}} = \frac{\partial}{\partial t_1}\left(\frac{\partial x_1^{+,k}}{\partial x_1^{+,p}}\right) = \frac{\partial[\Phi^{k,p}_{(t_1,t_1)}(\boldsymbol{x}_1^+)]}{\partial t_1} = \dot{\Phi}^{k,p}_{(t_1,t_1)}(\boldsymbol{x}_1^+) = \frac{\partial y^k(\boldsymbol{x}_1^+, t_1)}{\partial x_1^{+,p}}\,. \tag{21}$$

The deviation of the virtual state $\delta \boldsymbol{x}_1^*$ can be obtained by applying a reversion of series on Eq. (18), which is given as

$$\delta x_1^{*,k} = \delta x_1^{-,k} + \delta\Delta x_1^k - f_+^k \delta t_1 - \frac{1}{2} g_+^k \delta t_1 \delta t_1 + H_+^{k,p} f_+^p \delta t_1 \delta t_1 - H_+^{k,p} \delta t_1 (\delta x_1^{-,p} + \delta\Delta x_1^p) . \tag{22}$$

Equation (22) is the obtained second-order orbit propagator for the second segment. Then we connect the propagators in the first segment and the second segment. By substituting Eqs. (13)-(16) into Eq. (22) and comprising linear and quadratic terms, Eq. (22) can be rewritten as

$$\delta x_1^{*,k} = A_1^{k,p} \delta x_0^p + B_1^k \delta t_1 + \delta\Delta x_1^k + \frac{1}{2} A_2^{k,p_1 p_2} \delta x_0^{p_1} \delta x_0^{p_2} + \frac{1}{2} B_2^k \delta t_1 \delta t_1 + C^{k,p} \delta x_0^p \delta t_1 + D^{k,p} \delta\Delta x_1^p \delta t_1 , \tag{23}$$

where $A_1^{k,p} = \Phi_{(t_0,t_1)}^{k,p}$, $A_2^{k,p_1 p_2} = \Psi_{(t_0,t_1)}^{k,p_1 p_2}$, $B_1^k = f_-^k - f_+^k$, $B_2^k = g_-^k - g_+^k + 2H_+^{k,p} f_+^p - 2H_+^{k,p} f_-^p$, $C^{k,p} = H_-^{k,p} - H_+^{k,l} \Phi_{(t_0,t_1)}^{l,p}$ and $D^{k,p} = -H_+^{k,p}$.

Finally, we investigate the propagation in the third segment. Similar to Eq. (11), in the period $t_1 \le t \le t_2$, the deviation $\delta \boldsymbol{x}(t)$ can be approximated as

$$\delta x^i(t) = \Phi_{(t_1,t)}^{i,k} \delta x_1^{*,k} + \frac{1}{2} \Psi_{(t_1,t)}^{i,k_1 k_2} \delta x_1^{*,k_1} \delta x_1^{*,k_2} , \tag{24}$$

which, after substituting for $\boldsymbol{x}_1^*$ from Eq. (23), yields

$$\begin{aligned} \delta x^i(t) = & \underbrace{\Phi_{(t_1,t)}^{i,k} A_1^{k,p} \delta x_0^p + \frac{1}{2} (\Phi_{(t_1,t)}^{i,k} A_2^{k,p_1 p_2} + \Psi_{(t_1,t)}^{i,k_1 k_2} A_1^{k_1,p_1} A_1^{k_2,p_2}) \delta x_0^{p_1} \delta x_0^{p_2}}_{\boldsymbol{T}(\delta \boldsymbol{x}_0)} \\ & + \underbrace{\Phi_{(t_1,t)}^{i,k} B_1^k \delta t_1 + \frac{1}{2} (\Phi_{(t_1,t)}^{i,k} B_2^k + \Psi_{(t_1,t)}^{i,k_1 k_2} B_1^{k_1} B_1^{k_2}) \delta t_1 \delta t_1}_{\boldsymbol{T}(\delta t_1)} + \underbrace{\Phi_{(t_1,t)}^{i,k} \delta\Delta x_1^k + \frac{1}{2} \Psi_{(t_1,t)}^{i,k_1 k_2} \delta\Delta x_1^{k_1} \delta\Delta x_1^{k_2}}_{\boldsymbol{T}(\delta\Delta \boldsymbol{x}_1)} \\ & + \underbrace{(\Phi_{(t_1,t)}^{i,k_1} C^{k_1,p_1} + \Psi_{(t_1,t)}^{i,k_1 k_2} A_1^{k_1,p_1} B_1^{k_2}) \delta x_0^{p_1} \delta t_1}_{\boldsymbol{T}(\delta \boldsymbol{x}_0, \delta t_1)} + \underbrace{\Psi_{(t_1,t)}^{i,k_1 k_2} A_1^{k_1,p_1} I_6^{k_2,p_2} \delta x_0^{p_1} \delta\Delta x_1^{p_2}}_{\boldsymbol{T}(\delta \boldsymbol{x}_0, \delta\Delta \boldsymbol{x}_1)} + \underbrace{\Psi_{(t_1,t)}^{i,k_1 k_2} B_1^{k_1} \delta\Delta x_1^{k_2} \delta t_1}_{\boldsymbol{T}(\delta\Delta \boldsymbol{x}_1, \delta t_1)} \end{aligned} , \tag{25}$$

where $\boldsymbol{I}_6$ is a 6-dimensional identity matrix; $I_6^{k_2,p_2}$ is the element in row k_2 and column p_2, and $\boldsymbol{T}(\bullet)$ is the independent term of the corresponding variables. One can see from Eqs. (23) and (24) that the virtual state $\boldsymbol{x}_1^*$ is an important variable in the developed modified STT. Although the virtual state $\boldsymbol{x}_1^*$ is finally removed from the equations (as shown in Eq. (25)), it helps build a relationship between $\delta \boldsymbol{x}(t)$ ($t > t_1$) and $\delta \boldsymbol{x}_0$, $\delta\Delta \boldsymbol{v}_1$ and δt_1. The difficulty of developing such a modified STT lies in the coupling effects of $\delta\Delta \boldsymbol{v}_1$ and δt_1 on orbit deviations. By

introducing the virtual state, the proposed modified STT can independently and sequentially address the effects of $\delta\Delta\boldsymbol{v}_1$ (using Eq. (17)) and δt_1 (using Eqs. (21)-(23)).

Equation (25) is the obtained second-order solution for orbit propagation. For convenience, let $\delta\boldsymbol{X}=[\delta\boldsymbol{x}_0;\delta\Delta\boldsymbol{v}_1;\delta t_1]$ be the deviation of the estimation parameter vector. Then, rewrite Eqs. (11) and (25) as

$$\delta\boldsymbol{x}(t)=\boldsymbol{\Phi}(t)\delta\boldsymbol{X}+\frac{1}{2}\boldsymbol{\Psi}(t)\otimes\delta\boldsymbol{X}\otimes\delta\boldsymbol{X}\,, \tag{26}$$

where $\boldsymbol{\Phi}\in\mathbb{R}^{6\times10}$ and $\boldsymbol{\Psi}\in\mathbb{R}^{6\times10\times10}$ denote the proposed modified first-order and second-order STTs, respectively, and the operator $\otimes$ denotes the Kronecker tensor product.

During $[t_0,t_1]$, the modified STTs $\boldsymbol{\Phi}(t)$ and $\boldsymbol{\Psi}(t)$ are given as

$$\boldsymbol{\Phi}^{i,:}(t)=\left[\begin{array}{ccc|c|c}\Phi^{i,1}_{(t_0,t)} & \cdots & \Phi^{i,6}_{(t_0,t)} & \boldsymbol{0}_{1\times3} & \boldsymbol{0}_{1\times1}\end{array}\right], \tag{27}$$

$$\boldsymbol{\Psi}^{i,:,:}(t)=\left[\begin{array}{ccc|c|c}\Psi^{i,1,1}_{(t_0,t)} & \cdots & \Psi^{i,1,6}_{(t_0,t)} & \boldsymbol{0}_{6\times3} & \boldsymbol{0}_{6\times1}\\ \vdots & \ddots & \vdots & & \\ \Psi^{i,6,1}_{(t_0,t)} & \cdots & \Psi^{i,6,6}_{(t_0,t)} & & \\ \hline \multicolumn{3}{c|}{\boldsymbol{0}_{3\times6}} & \boldsymbol{0}_{3\times3} & \boldsymbol{0}_{3\times1}\\ \hline \multicolumn{3}{c|}{\boldsymbol{0}_{1\times6}} & \boldsymbol{0}_{1\times3} & \boldsymbol{0}_{1\times1}\end{array}\right]. \tag{28}$$

During $[t_1,t_2]$, the modified STTs $\boldsymbol{\Phi}(t)$ and $\boldsymbol{\Psi}(t)$ are partitioned as

$$\boldsymbol{\Phi}^{i,:}(t)=\left[\begin{array}{ccc|ccc}\Phi^{i,k}_{(t_1,t)}A_1^{k,1} & \cdots & \Phi^{i,k}_{(t_1,t)}A_1^{k,6} & \Phi^{i,4}_{(t_1,t)} & \cdots & \Phi^{i,6}_{(t_1,t)}\end{array}\right|\left.\Phi^{i,k}_{(t_1,t)}B_1^{k}\right], \tag{29}$$

$$\boldsymbol{\Psi}^{i,:,:}(t)=\left[\begin{array}{ccc|ccc|c}\Psi^{i,k_1k_2}_{(t_1,t)}A_1^{k_1,1}A_1^{k_2,1}+\Phi^{i,k}_{(t_1,t)}A_2^{k,1,1} & \cdots & \Psi^{i,k_1k_2}_{(t_1,t)}A_1^{k_1,1}A_1^{k_2,6}+\Phi^{i,k}_{(t_1,t)}A_2^{k,1,6} & \Psi^{i,k_1k_2}_{(t_1,t)}A_1^{k_1,1}I_6^{k_2,4} & \cdots & \Psi^{i,k_1k_2}_{(t_1,t)}A_1^{k_1,1}I_6^{k_2,6} & \Psi^{i,k_1k_2}_{(t_1,t)}A_1^{k_1,1}B_1^{k_2}+\Phi^{i,k_1}_{(t_1,t)}C^{k_1,1}\\ \vdots & \ddots & \vdots & \vdots & \ddots & \vdots & \vdots\\ \Psi^{i,k_1k_2}_{(t_1,t)}A_1^{k_1,6}A_1^{k_2,1}+\Phi^{i,k}_{(t_1,t)}A_2^{k,6,1} & \cdots & \Psi^{i,k_1k_2}_{(t_1,t)}A_1^{k_1,6}A_1^{k_2,6}+\Phi^{i,k}_{(t_1,t)}A_2^{k,6,6} & \Psi^{i,k_1k_2}_{(t_1,t)}A_1^{k_1,6}I_6^{k_2,4} & \cdots & \Psi^{i,k_1k_2}_{(t_1,t)}A_1^{k_1,6}I_6^{k_2,6} & \Psi^{i,k_1k_2}_{(t_1,t)}A_1^{k_1,6}B_1^{k_2}+\Phi^{i,k_1}_{(t_1,t)}C^{k_1,6}\\ \hline \Psi^{i,k_1k_2}_{(t_1,t)}A_1^{k_1,1}I_6^{k_2,4} & \cdots & \Psi^{i,k_1k_2}_{(t_1,t)}A_1^{k_1,6}I_6^{k_2,4} & \Psi^{i,4,4}_{(t_1,t)} & \cdots & \Psi^{i,4,6}_{(t_1,t)} & \Psi^{i,k_1,4}_{(t_1,t)}B_1^{k_1}\\ \vdots & \ddots & \vdots & \vdots & \ddots & \vdots & \vdots\\ \Psi^{i,k_1k_2}_{(t_1,t)}A_1^{k_1,1}I_6^{k_2,6} & \cdots & \Psi^{i,k_1k_2}_{(t_1,t)}A_1^{k_1,6}I_6^{k_2,6} & \Psi^{i,6,4}_{(t_1,t)} & \cdots & \Psi^{i,6,6}_{(t_1,t)} & \Psi^{i,k_1,6}_{(t_1,t)}B_1^{k_1}\\ \hline \Psi^{i,k_1k_2}_{(t_1,t)}A_1^{k_1,1}B_1^{k_2}+\Phi^{i,k_1}_{(t_1,t)}C^{k_1,1} & \cdots & \Psi^{i,k_1k_2}_{(t_1,t)}A_1^{k_1,6}B_1^{k_2}+\Phi^{i,k_1}_{(t_1,t)}C^{k_1,6} & \Psi^{i,k_1,4}_{(t_1,t)}B_1^{k_1} & \cdots & \Psi^{i,k_1,6}_{(t_1,t)}B_1^{k_1} & \Psi^{i,k_1k_2}_{(t_1,t)}B_1^{k_1}B_1^{k_2}+\Phi^{i,k}_{(t_1,t)}B_2^{k}\end{array}\right]. \tag{30}$$

A summary of processes in Eqs. (11)-(30) is provided in Algorithm 1. The pseudo-code presented herein is used to clearly describe the derivation process of Eqs. (11)-(30). It doesn't mean that the modified STTs are repeatedly computed when predicting the orbit state deviation $\delta\boldsymbol{x}(t)$. In practice, once the modified STTs are obtained, the

orbit state deviation $\delta \boldsymbol{x}(t)$ can be analytically predicted without additional numerical integrations. It should also be noted that in Eq. (23), the deviation of the virtual state $\delta \boldsymbol{x}_1^*$, rather than the deviation of the true state $\delta \boldsymbol{x}(t_1)$, is predicted. The residual between $\delta \boldsymbol{x}_1^*$ and $\delta \boldsymbol{x}(t_1)$, *i.e.*, the difference between the red line and green dot in Fig. 1, is neglected by the proposed modified STT (Eqs. (26)-(30)). Therefore, the accuracy of the proposed modified STT slightly degrades around the epoch t_1. The accuracy performance of the proposed modified STT around the epoch t_1 will be discussed in Sec. IV.A.

Algorithm 1: Pseudo-code of calculating the modified STT

Inputs: initial epoch t_0, final epoch t_2, reference variables $\boldsymbol{x}_0$, t_1 and $\Delta \boldsymbol{v}_1$, and the deviations $\delta \boldsymbol{x}_0$, δt_1 and $\delta \Delta \boldsymbol{v}_1$

Output: the orbit state deviation $\delta \boldsymbol{x}(t)$ at any given epoch t ($t \in [t_0, t_1]$), and the modified STTs $\boldsymbol{\Phi}(t)$ and $\boldsymbol{\Psi}(t)$

1 Integrate the STTs $\Phi_{(t_0,t)}^{k,p}$ and $\Psi_{(t_0,t)}^{k,p_1p_2}$ using Eqs. (8)-(10).
2 Predict $\delta \boldsymbol{x}(t)$ ($t \in [t_0, t_1]$) and $\delta \boldsymbol{x}(t_1)$ using Eqs. (11) and (12).
3 Calculate $\delta \boldsymbol{x}_1^-$ using Eqs. (13)-(16).
4 Calculate $\delta \boldsymbol{x}_1^+$ using Eqs. (18)-(21).
5 Calculate the virtual state deviation $\delta \boldsymbol{x}_1^*$ using Eq. (23).
6 Predict $\delta \boldsymbol{x}(t)$ ($t \in [t_1, t_2]$) using Eq. (25).
7 Calculate the modified STTs $\boldsymbol{\Phi}(t)$ and $\boldsymbol{\Psi}(t)$ using Eqs. (27)-(30).

B. Second-order measurement model

Equations (26)-(30) present the relationship between the deviations of the estimation parameter vector $\delta \boldsymbol{X}$ and $\delta \boldsymbol{x}(t)$. In this subsection, the transformation from the deviation of the estimation parameter vector $\delta \boldsymbol{X}$ to the deviation of the measurement $\delta \boldsymbol{z}(t)$ at any future epoch t, is derived. According to Eq. (2), the measurement deviation $\delta \boldsymbol{z}(t)$ can be approximated using a second-order Taylor series as

$$\delta \boldsymbol{z}(t) = \boldsymbol{U}(t)\delta \boldsymbol{x}(t) + \frac{1}{2}\boldsymbol{Q}(t) \otimes \delta \boldsymbol{x}(t) \otimes \delta \boldsymbol{x}(t), \tag{31}$$

where

$$U^{i,k}(t) = \frac{\partial h^i(\boldsymbol{x}(t))}{\partial x^k(t)}, \tag{32}$$

$$Q^{i,k_1k_2}(t) = \frac{\partial^2 h^i(\boldsymbol{x}(t))}{\partial x^{k_1}(t)\partial x^{k_2}(t)}. \tag{33}$$

Substituting Eq. (26) into Eq. (31) and neglecting higher-order terms,

$$\delta \boldsymbol{z}(t) = \boldsymbol{U}(t)\boldsymbol{\Phi}(t)\delta \boldsymbol{X} + \frac{1}{2}\boldsymbol{U}(t)\left[\boldsymbol{\Psi}(t) \otimes \delta \boldsymbol{X} \otimes \delta \boldsymbol{X}\right] + \frac{1}{2}\boldsymbol{Q}(t) \otimes \left(\boldsymbol{\Phi}(t)\delta \boldsymbol{X}\right) \otimes \left(\boldsymbol{\Phi}(t)\delta \boldsymbol{X}\right). \tag{34}$$

Equation (34) can be further simplified as

$$\delta \boldsymbol{z}(t) = \boldsymbol{\Xi}(t)\delta \boldsymbol{X} + \frac{1}{2}\boldsymbol{\Theta}(t) \otimes \delta \boldsymbol{X} \otimes \delta \boldsymbol{X} \,, \tag{35}$$

where

$$\Xi^{i,p}(t) = U^{i,k}(t)\Phi^{k,p}(t) \,, \tag{36}$$

$$\Theta^{i,p_1p_2}(t) = U^{i,j}(t)\Psi^{j,p_1p_2}(t) + Q^{i,k_1k_2}(t)\Phi^{k_1,p_1}(t)\Phi^{k_2,p_2}(t) \,. \tag{37}$$

Equations (35)-(37) are the derived second-order models that transform from the deviation of the estimation parameter vector $\delta \boldsymbol{X}$ to the measurement deviation $\delta \boldsymbol{z}(t)$. Assume that the estimation parameter vector deviation $\delta \boldsymbol{X}$ is a zero-mean random vector, and its covariance matrix is represented by $\boldsymbol{P} = [P^{ab}]_{10\times 10}$. The mean $\boldsymbol{m}(\delta \boldsymbol{z}(t)) = [m^i(\delta \boldsymbol{z}(t))]_{d\times 1}$ and covariance matrix $\boldsymbol{P}(\delta \boldsymbol{z}(t)) = [P^{ij}(\delta \boldsymbol{z}(t))]_{d\times d}$ of the measurement deviation $\delta \boldsymbol{z}(t)$ are then given as

$$m^i(\delta \boldsymbol{z}(t)) = \frac{1}{2}\sum_{a=1}^{n}\sum_{b=1}^{n}\Theta^{i,ab}(t)P^{ab} \,, \tag{38}$$

$$\begin{aligned} P^{ij}(\delta \boldsymbol{z}(t)) = &\sum_{a=1}^{10}\sum_{\alpha=1}^{10}\Xi^{i,a}(t)\Xi^{j,\alpha}(t)P^{a\alpha} - m^i(\delta \boldsymbol{z}(t))m^j(\delta \boldsymbol{z}(t)) \\ &+\frac{1}{4}\sum_{a=1}^{10}\sum_{b=1}^{10}\sum_{a=1}^{10}\sum_{\beta=1}^{10}\Theta^{i,ab}(t)\Theta^{j,\alpha\beta}(t)[P^{ab}P^{\alpha\beta} + P^{a\alpha}P^{b\beta} + P^{a\beta}P^{b\alpha}] \end{aligned} \,. \tag{39}$$

For the sake of simplicity, the nonlinear covariance propagations in Eqs. (38) and (39) are denoted as

$$[\boldsymbol{m}(\delta \boldsymbol{z}(t)), \boldsymbol{P}(\delta \boldsymbol{z}(t))] = \text{Propagation}(\boldsymbol{P}, \boldsymbol{\Xi}(t), \boldsymbol{\Theta}(t)) \,. \tag{40}$$

C. Second-order optimal estimation

Starting from a priori estimations (obtained from initial, or prior orbit determination), the reference orbit can be propagated using the modified STT in Eqs. (26), and the residuals between the incoming observation data and the predicted measurements are obtained. Based on the partial derivatives of the measurements with respect to the estimation parameter vector $\boldsymbol{X}$ in Eqs. (35)-(37), a priori estimations can be corrected.

Assume that in the period $[t_0, t_2]$, K observations are obtained using the equipped sensor. The K observations are labeled by

$$\tilde{\boldsymbol{z}}(\tau_j) = \boldsymbol{h}(\tilde{\boldsymbol{x}}(\tau_j)) + \boldsymbol{\varepsilon},\ j \in \{1, 2, \cdots, K\} \,, \tag{41}$$

where $t_0 \le \tau_1 < \tau_2 < \cdots < \tau_{K-1} < \tau_K \le t_2$ are the epoch series when the observations are received. Note that the reference orbit state $\boldsymbol{x}(t)$ can be computed based on the current estimation $\boldsymbol{X} = [\boldsymbol{x}_0; \Delta\boldsymbol{v}_1; t_1]$. The predicted measurement $\boldsymbol{z}(\tau_i) = \boldsymbol{h}(\boldsymbol{x}(\tau_i))$ is then calculated using the reference orbit state $\boldsymbol{x}(\tau_i)$ and the measurement model in Eq. (2). Thus, the residuals of the K observations are written as

$$\delta\boldsymbol{Z} = \begin{bmatrix} \delta\boldsymbol{z}(\tau_1) \\ \delta\boldsymbol{z}(\tau_2) \\ \vdots \\ \delta\boldsymbol{z}(\tau_K) \end{bmatrix} = \begin{bmatrix} \tilde{\boldsymbol{z}}(\tau_1) - \boldsymbol{z}(\tau_1) \\ \tilde{\boldsymbol{z}}(\tau_2) - \boldsymbol{z}(\tau_2) \\ \vdots \\ \tilde{\boldsymbol{z}}(\tau_K) - \boldsymbol{z}(\tau_K) \end{bmatrix} = \delta\boldsymbol{h} + \boldsymbol{\varepsilon} = \begin{bmatrix} \boldsymbol{h}(\tilde{\boldsymbol{x}}(\tau_1)) - \boldsymbol{h}(\boldsymbol{x}(\tau_1)) \\ \boldsymbol{h}(\tilde{\boldsymbol{x}}(\tau_2)) - \boldsymbol{h}(\boldsymbol{x}(\tau_2)) \\ \vdots \\ \boldsymbol{h}(\tilde{\boldsymbol{x}}(\tau_K)) - \boldsymbol{h}(\boldsymbol{x}(\tau_K)) \end{bmatrix} + \begin{bmatrix} \boldsymbol{\varepsilon}_1 \\ \boldsymbol{\varepsilon}_2 \\ \vdots \\ \boldsymbol{\varepsilon}_K \end{bmatrix}, \tag{42}$$

where $\boldsymbol{\varepsilon}_i \in \mathbb{R}^d$ is the measurement noise of the *i*-th observation.

Let $\delta\boldsymbol{X} \in \mathbb{R}^{10}$ be the deviation between the real state $\tilde{\boldsymbol{X}} = [\tilde{\boldsymbol{x}}_0; \Delta\tilde{\boldsymbol{v}}_1; \tilde{t}_1] \in \mathbb{R}^{10}$ and the current estimation $\boldsymbol{X}$. According to Eqs. (31)-(37), $\delta\boldsymbol{h}$ can be approximated using a series of second-order expressions as

$$\delta\boldsymbol{h} = \delta\boldsymbol{Z}' = \begin{bmatrix} \delta\boldsymbol{z}'(\tau_1) \\ \delta\boldsymbol{z}'(\tau_2) \\ \vdots \\ \delta\boldsymbol{z}'(\tau_K) \end{bmatrix} = \begin{bmatrix} \boldsymbol{\Xi}(\tau_1)\delta\boldsymbol{X} + \frac{1}{2}\boldsymbol{\Theta}(\tau_1) \otimes \delta\boldsymbol{X} \otimes \delta\boldsymbol{X} \\ \boldsymbol{\Xi}(\tau_2)\delta\boldsymbol{X} + \frac{1}{2}\boldsymbol{\Theta}(\tau_2) \otimes \delta\boldsymbol{X} \otimes \delta\boldsymbol{X} \\ \vdots \\ \boldsymbol{\Xi}(\tau_K)\delta\boldsymbol{X} + \frac{1}{2}\boldsymbol{\Theta}(\tau_K) \otimes \delta\boldsymbol{X} \otimes \delta\boldsymbol{X} \end{bmatrix}. \tag{43}$$

The expression of $\delta\boldsymbol{Z}'$ in Eq. (43) can be further simplified as

$$\delta\boldsymbol{Z}' = \boldsymbol{\Omega}\delta\boldsymbol{X} + \frac{1}{2}\boldsymbol{\Sigma} \otimes \delta\boldsymbol{X} \otimes \delta\boldsymbol{X}, \tag{44}$$

where

$$\boldsymbol{\Omega}^{:,p} = [\boldsymbol{\Xi}^{:,p}(\tau_1); \boldsymbol{\Xi}^{:,p}(\tau_2); \cdots; \boldsymbol{\Xi}^{:,p}(\tau_K)], \tag{45}$$

$$\boldsymbol{\Sigma}^{:,p_1p_2} = [\boldsymbol{\Theta}^{:,p_1p_2}(\tau_1); \boldsymbol{\Theta}^{:,p_1p_2}(\tau_2); \cdots; \boldsymbol{\Theta}^{:,p_1p_2}(\tau_K)]. \tag{46}$$

In this paper, the goal of the OD of the spacecraft under an impulsive maneuver is to determine the optimal $\delta\boldsymbol{X}$ that can minimize the deviation between $\delta\boldsymbol{Z}$ and $\delta\boldsymbol{Z}'$. In the remainder of this subsection, the second-order optimal estimation, extended from the conventional least-squares solution, is presented to solve the impulsive OD method.

Substituting Eqs. (43) and (44) into Eq. (42) yields

$$\delta\boldsymbol{Z} = \delta\boldsymbol{h} + \boldsymbol{\varepsilon} = \boldsymbol{\Omega}\delta\boldsymbol{X} + \frac{1}{2}\boldsymbol{\Sigma} \otimes \delta\boldsymbol{X} \otimes \delta\boldsymbol{X} + \boldsymbol{\varepsilon}. \tag{47}$$

First, the weights of each term should be determined. Note that the covariance matrix of $\delta \boldsymbol{z}'(\tau_i)$ is

$$\boldsymbol{P}_i' = \text{Propagation}(\boldsymbol{P}(\delta \boldsymbol{X}), \boldsymbol{\Xi}(\tau_i), \boldsymbol{\Theta}(\tau_i)), \tag{48}$$

which can be obtained using Eqs. (38) and (39). Thus, the uncertainty of $\delta \boldsymbol{z}(\tau_i) - \delta \boldsymbol{z}'(\tau_i)$ can be represented by a covariance matrix $\boldsymbol{P}_i$ as

$$\boldsymbol{P}_i = \boldsymbol{P}_i' + \boldsymbol{R}. \tag{49}$$

Thus, the weights matrix $\boldsymbol{W}$ is represented by

$$\boldsymbol{W} = \begin{bmatrix} \boldsymbol{P}_1 & \boldsymbol{0}_{d\times(K-2)d} & \boldsymbol{0}_{d\times d} \\ \boldsymbol{0}_{(K-2)d\times d} & \ddots & \boldsymbol{0}_{(K-2)d\times d} \\ \boldsymbol{0}_{d\times d} & \boldsymbol{0}_{d\times(K-2)d} & \boldsymbol{P}_k \end{bmatrix}^{-1}. \tag{50}$$

To avoid a numerical singularity when obtaining the optimal solution, $\boldsymbol{W}$ can be normalized as $\boldsymbol{W}/\|\boldsymbol{W}\|$ when solving the OD problem. Combining Eqs. (42)-(44) with Eq. (50), the performance metric to be minimized is defined as

$$\begin{aligned} J &= \left(\delta \boldsymbol{Z} - \boldsymbol{\Omega}\delta \boldsymbol{X} - \frac{1}{2}\boldsymbol{\Sigma}\otimes\delta \boldsymbol{X}\otimes\delta \boldsymbol{X}\right)^T \boldsymbol{W}\left(\delta \boldsymbol{Z} - \boldsymbol{\Omega}\delta \boldsymbol{X} - \frac{1}{2}\boldsymbol{\Sigma}\otimes\delta \boldsymbol{X}\otimes\delta \boldsymbol{X}\right) \\ &= \text{Tr}\left(\left(\delta \boldsymbol{Z} - \boldsymbol{\Omega}\delta \boldsymbol{X} - \frac{1}{2}\boldsymbol{\Sigma}\otimes\delta \boldsymbol{X}\otimes\delta \boldsymbol{X}\right)\boldsymbol{W}^T\left(\delta \boldsymbol{Z} - \boldsymbol{\Omega}\delta \boldsymbol{X} - \frac{1}{2}\boldsymbol{\Sigma}\otimes\delta \boldsymbol{X}\otimes\delta \boldsymbol{X}\right)^T\right). \end{aligned} \tag{51}$$

Similar to the deviation of the LSM, the partial derivative of the metrics J can be obtained by

$$\frac{\partial J}{\partial \boldsymbol{X}} = -2\boldsymbol{\Gamma}^T\boldsymbol{W}\left(\delta \boldsymbol{Z} - \boldsymbol{\Omega}\delta \boldsymbol{X} - \frac{1}{2}\boldsymbol{\Sigma}\otimes\delta \boldsymbol{X}\otimes\delta \boldsymbol{X}\right), \tag{52}$$

where

$$\Gamma^{i,k} = \Omega^{i,k} + \Sigma^{i,kp}\delta X^p. \tag{53}$$

The optimal estimation $\delta \boldsymbol{X}$ can be obtained by solving the equation $\partial J/\partial \boldsymbol{X} = \boldsymbol{0}_{1\times 10}$. However, the solution cannot be directly computed as Eq. (52) is a high-order system. A method to obtain the second-order optimal estimation of $\delta \boldsymbol{X}$ is therefore proposed herein.

Neglecting the second-order terms of Eq. (44), the performance metric J is rewritten as

$$\overline{J} = \left(\delta \boldsymbol{Z} - \boldsymbol{\Omega}\delta \boldsymbol{X}\right)^T \boldsymbol{W}\left(\delta \boldsymbol{Z} - \boldsymbol{\Omega}\delta \boldsymbol{X}\right) = \text{Tr}\left(\left(\delta \boldsymbol{Z} - \boldsymbol{\Omega}\delta \boldsymbol{X}\right)\boldsymbol{W}^T\left(\delta \boldsymbol{Z} - \boldsymbol{\Omega}\delta \boldsymbol{X}\right)^T\right). \tag{54}$$

where $\overline{J}$ is the performance metric containing only first-order terms.

By solving the equation $\partial \overline{J} / \partial \boldsymbol{X} = \mathbf{0}_{1\times 10}$, a first-order (linear) optimal solution is obtained by

$$\delta \overline{\boldsymbol{X}} = (\boldsymbol{\Omega}^T \boldsymbol{W} \boldsymbol{\Omega})^{-1} \boldsymbol{\Omega}^T \boldsymbol{W} \delta \boldsymbol{Z} . \tag{55}$$

Substituting the first-order solution into Eq. (53), the first-order approximation of $\boldsymbol{\Gamma}$ is calculated as

$$\overline{\Gamma}^{i,k} = \Omega^{i,k} + \Sigma^{i,kp} \delta \overline{X}^p . \tag{56}$$

Substituting the approximation in Eq. (56) into the partial derivative of the metrics J, Eq. (52) is written as

$$\frac{\partial J}{\partial \boldsymbol{X}} = -2\overline{\boldsymbol{\Gamma}}^T \boldsymbol{W} \left(\delta \boldsymbol{Z} - \boldsymbol{\Omega} \delta \boldsymbol{X} - \frac{1}{2} \boldsymbol{\Sigma} \otimes \delta \boldsymbol{X} \otimes \delta \boldsymbol{X} \right) = \mathbf{0}_{1\times 10} . \tag{57}$$

Similar to the operations in Eqs. (34)-(37), Eq. (57) can be simplified as

$$\delta \overline{\boldsymbol{Z}} - \overline{\boldsymbol{\Omega}} \delta \boldsymbol{X} - \frac{1}{2} \overline{\boldsymbol{\Sigma}} \otimes \delta \boldsymbol{X} \otimes \delta \boldsymbol{X} = \mathbf{0}_{1\times 10} , \tag{58}$$

where

$$\delta \overline{Z}^i = -2\overline{\Gamma}^{ji} W^{jk} \delta Z^k , \tag{59}$$

$$\overline{\Omega}^{i,p} = -2\overline{\Gamma}^{ji} W^{jk} \Omega^{kp} , \tag{60}$$

$$\overline{\Sigma}^{i,p_1 p_2} = -2\overline{\Gamma}^{ji} W^{jk} \Sigma^{k,p_1 p_2} . \tag{61}$$

According to Turner's method of series reversion [45], the solution of Eq. (58) is approximated by

$$\delta \hat{\boldsymbol{X}} = \overline{\boldsymbol{\Omega}}^{-1} \delta \overline{\boldsymbol{Z}} - \frac{1}{2} \overline{\boldsymbol{\Omega}}^{-1} \left[\overline{\boldsymbol{\Sigma}} \otimes \left(\overline{\boldsymbol{\Omega}}^{-1} \delta \overline{\boldsymbol{Z}} \right) \otimes \left(\overline{\boldsymbol{\Omega}}^{-1} \delta \overline{\boldsymbol{Z}} \right) \right] , \tag{62}$$

where $\delta \hat{\boldsymbol{X}}$ is the approximated second-order optimal estimation. Eq. (62) is the proposed second-order optimal estimation of the parameter of interest. Using Eq. (62), the estimation $\boldsymbol{X}$ can be corrected as $\boldsymbol{X} \leftarrow \boldsymbol{X} + \delta \hat{\boldsymbol{X}}$.

Comprising only linear and quadratic terms, the associated covariance matrix of the estimation $\delta \hat{\boldsymbol{X}}$ is given as

$$\boldsymbol{P}(\delta \hat{\boldsymbol{X}}) = \boldsymbol{E}[(\delta \boldsymbol{X} - \delta \hat{\boldsymbol{X}})(\delta \boldsymbol{X} - \delta \hat{\boldsymbol{X}})^T] . \tag{63}$$

Substitution of Eq. (62)into Eq. (63) results in

$$\delta \boldsymbol{X} - \delta \hat{\boldsymbol{X}} = \delta \boldsymbol{X} - \overline{\boldsymbol{\Omega}}^{-1} \delta \overline{\boldsymbol{Z}} + \frac{1}{2} \overline{\boldsymbol{\Omega}}^{-1} \left[\overline{\boldsymbol{\Sigma}} \otimes \left(\overline{\boldsymbol{\Omega}}^{-1} \delta \overline{\boldsymbol{Z}} \right) \otimes \left(\overline{\boldsymbol{\Omega}}^{-1} \delta \overline{\boldsymbol{Z}} \right) \right] . \tag{64}$$

Substitute Eq. (47) into Eq. (64), and reserve only the first- and second-order terms. Then $\delta \boldsymbol{X} - \delta \hat{\boldsymbol{X}}$ can be expressed as

$$
\begin{aligned}
\delta \boldsymbol{X} - \delta \hat{\boldsymbol{X}} &= \delta \boldsymbol{X} - (\bar{\boldsymbol{\Gamma}}^T \boldsymbol{W} \boldsymbol{\Omega})^{-1} \bar{\boldsymbol{\Gamma}}^T \boldsymbol{W} \delta \boldsymbol{Z} \\
&\quad + \frac{1}{2} (\bar{\boldsymbol{\Gamma}}^T \boldsymbol{W} \boldsymbol{\Omega})^{-1} \left\{ \bar{\boldsymbol{\Gamma}}^T \boldsymbol{W} \boldsymbol{\Sigma} \otimes \left[(\bar{\boldsymbol{\Gamma}}^T \boldsymbol{W} \boldsymbol{\Omega})^{-1} \bar{\boldsymbol{\Gamma}}^T \boldsymbol{W} \delta \boldsymbol{Z} \right] \otimes \left[(\bar{\boldsymbol{\Gamma}}^T \boldsymbol{W} \boldsymbol{\Omega})^{-1} \bar{\boldsymbol{\Gamma}}^T \boldsymbol{W} \delta \boldsymbol{Z} \right] \right\} \\
&= \delta \boldsymbol{X} - (\bar{\boldsymbol{\Gamma}}^T \boldsymbol{W} \boldsymbol{\Omega})^{-1} \bar{\boldsymbol{\Gamma}}^T \boldsymbol{W} (\boldsymbol{\Omega} \delta \boldsymbol{X} + \frac{1}{2} \boldsymbol{\Sigma} \otimes \delta \boldsymbol{X} \otimes \delta \boldsymbol{X} + \boldsymbol{\varepsilon}) \\
&\quad + \frac{1}{2} (\bar{\boldsymbol{\Gamma}}^T \boldsymbol{W} \boldsymbol{\Omega})^{-1} \left\{ \bar{\boldsymbol{\Gamma}}^T \boldsymbol{W} \boldsymbol{\Sigma} \otimes \left[\delta \boldsymbol{X} + (\bar{\boldsymbol{\Gamma}}^T \boldsymbol{W} \boldsymbol{\Omega})^{-1} \bar{\boldsymbol{\Gamma}}^T \boldsymbol{W} \boldsymbol{\varepsilon} \right] \otimes \left[\delta \boldsymbol{X} + (\bar{\boldsymbol{\Gamma}}^T \boldsymbol{W} \boldsymbol{\Omega})^{-1} \bar{\boldsymbol{\Gamma}}^T \boldsymbol{W} \boldsymbol{\varepsilon} \right] \right\}. \\
&= -(\bar{\boldsymbol{\Gamma}}^T \boldsymbol{W} \boldsymbol{\Omega})^{-1} \bar{\boldsymbol{\Gamma}}^T \boldsymbol{W} \boldsymbol{\varepsilon} + \frac{1}{2} (\bar{\boldsymbol{\Gamma}}^T \boldsymbol{W} \boldsymbol{\Omega})^{-1} \left\{ \bar{\boldsymbol{\Gamma}}^T \boldsymbol{W} \boldsymbol{\Sigma} \otimes \delta \boldsymbol{X} \otimes \left[(\bar{\boldsymbol{\Gamma}}^T \boldsymbol{W} \boldsymbol{\Omega})^{-1} \bar{\boldsymbol{\Gamma}}^T \boldsymbol{W} \boldsymbol{\varepsilon} \right] \right\} \\
&\quad + \frac{1}{2} (\bar{\boldsymbol{\Gamma}}^T \boldsymbol{W} \boldsymbol{\Omega})^{-1} \left\{ \bar{\boldsymbol{\Gamma}}^T \boldsymbol{W} \boldsymbol{\Sigma} \otimes \left[(\bar{\boldsymbol{\Gamma}}^T \boldsymbol{W} \boldsymbol{\Omega})^{-1} \bar{\boldsymbol{\Gamma}}^T \boldsymbol{W} \boldsymbol{\varepsilon} \right] \otimes \delta \boldsymbol{X} \right\} \\
&\quad + \frac{1}{2} (\bar{\boldsymbol{\Gamma}}^T \boldsymbol{W} \boldsymbol{\Omega})^{-1} \left\{ \bar{\boldsymbol{\Gamma}}^T \boldsymbol{W} \boldsymbol{\Sigma} \otimes \left[(\bar{\boldsymbol{\Gamma}}^T \boldsymbol{W} \boldsymbol{\Omega})^{-1} \bar{\boldsymbol{\Gamma}}^T \boldsymbol{W} \boldsymbol{\varepsilon} \right] \otimes \left[(\bar{\boldsymbol{\Gamma}}^T \boldsymbol{W} \boldsymbol{\Omega})^{-1} \bar{\boldsymbol{\Gamma}}^T \boldsymbol{W} \boldsymbol{\varepsilon} \right] \right\}
\end{aligned} \tag{65}
$$

Substituting the results in Eq. (65) into Eq. (63), the covariance matrix of the second-order estimation $\delta \hat{\boldsymbol{X}}$ is further given as

$$
\begin{aligned}
\boldsymbol{P}(\delta \hat{\boldsymbol{X}}) &= \mathbb{E} \left\{ \left[(\bar{\boldsymbol{\Gamma}}^T \boldsymbol{W} \boldsymbol{\Omega})^{-1} \bar{\boldsymbol{\Gamma}}^T \boldsymbol{W} \boldsymbol{\varepsilon} \right] \left[(\bar{\boldsymbol{\Gamma}}^T \boldsymbol{W} \boldsymbol{\Omega})^{-1} \bar{\boldsymbol{\Gamma}}^T \boldsymbol{W} \boldsymbol{\varepsilon} \right]^T \right\} = \mathbb{E} \left[(\bar{\boldsymbol{\Gamma}}^T \boldsymbol{W} \boldsymbol{\Omega})^{-1} \bar{\boldsymbol{\Gamma}} \boldsymbol{W} \boldsymbol{\varepsilon} \boldsymbol{\varepsilon}^T \boldsymbol{W}^T \bar{\boldsymbol{\Gamma}}^T (\boldsymbol{\Omega}^T \boldsymbol{W} \bar{\boldsymbol{\Gamma}})^{-1} \right] \\
&= (\bar{\boldsymbol{\Gamma}} \boldsymbol{W} \boldsymbol{\Omega})^{-1} \bar{\boldsymbol{\Gamma}}^T \boldsymbol{W} \boldsymbol{R} \boldsymbol{W}^T \bar{\boldsymbol{\Gamma}} (\boldsymbol{\Omega}^T \boldsymbol{W} \bar{\boldsymbol{\Gamma}})^{-1}
\end{aligned} \tag{66}
$$

Note that the second-order solution in Eq. (62) corresponds to one round of iteration. The estimations in one iteration are not sufficiently accurate. Thus, to achieve a certain threshold level, it is necessary to carry out multiple iterations so that the algorithm can converge. The convergence performance of the proposed method will be presented in the simulation section.

D. Overall procedure

A flow diagram outlining the overall procedure of the proposed method for orbit estimation and maneuver reconstruction is illustrated in Fig. 2. The inputs of the algorithm include the initial parameter estimation $\boldsymbol{X}^{(0)} = [\boldsymbol{x}_0^{(0)}; \Delta \boldsymbol{v}_1^{(0)}; t_1^{(0)}]$ and its associated covariance matrix $\boldsymbol{P}^0$, the K observations $\tilde{\boldsymbol{z}}(\tau_j)$ $j \in \{1, 2, \cdots, K\}$, and the covariance matrix of the measurement noise $\boldsymbol{R}$. The superscript (i) denotes the results of the i-th iteration. It differs from the previous superscripts that represent the elements (for example, the superscripts in Eqs. (59)-(61)) in that it has parentheses. The iterations terminate if the Frobenius norm of the optimal solution $\delta \hat{\boldsymbol{X}}^{(i-1)}$ is smaller than the predefined tolerance η, or the maximum iteration $i_{\max}$ is reached.

Note that the proposed method is based on the second-order modified STT (Eqs. (26)-(30)) and the second-order optimal solution (Eqs. (62) and (66)). The linear version of the solution can be found in Eq. (55). One of the

advantages of such a second-order model is that the coupling term of the epoch t_1 and the vector $\Delta \boldsymbol{v}_1$ is considered (the term $\boldsymbol{T}(\delta\Delta\boldsymbol{x}_1, \delta t_1)$ in Eq. (25)). The epoch and vector of the impulsive maneuver are critical to the impulsive maneuvering spacecraft OD problem; thus, considering the coupling term can improve accuracy and convergence of the algorithm. A comparison between the linear and second-order solutions will be given in Sec. IV.A.1.

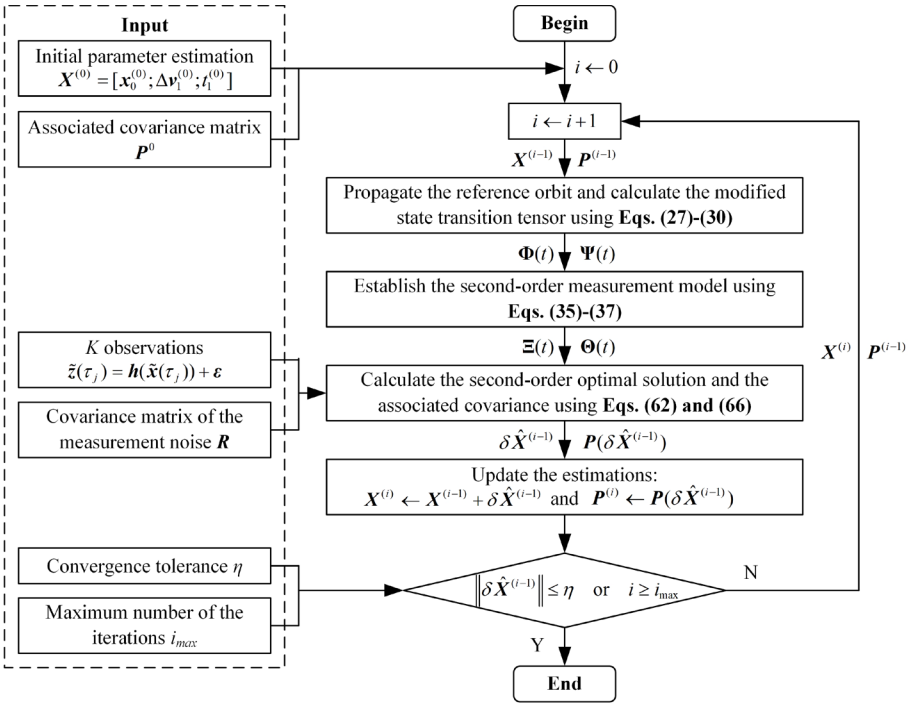

Fig. 2. A flow diagram of the proposed method.

IV. Numerical Simulations

To demonstrate protentional use cases for the equations derived in Sec. III, two simple applications, one in the low-Earth orbit (LEO) and the other in the geostationary orbit (GEO), are first studied. The orbit estimation and maneuver reconstruction performances of the proposed method are analyzed by comparing with several conventional maneuvering spacecraft OD algorithms. Then, sensitivity analyses are performed to investigate the influences of the initial guess, magnitude of the maneuver, and measurement interval on method performances.

A. Estimated accuracy analysis

1. LEO testing case

Consider two spacecraft in low-Earth orbit, with one being the target and the other being the observer. The nominal orbit elements of the target spacecraft and observer spacecraft are listed in Table 1, where h, e, n, i, ω

and Ω label the altitude at apogee, eccentricity, true anomaly, inclination, argument of periapsis, and longitude of the ascending node, respectively.

Table 1 Nominal orbit elements of the target and the observer in the LEO testing case

Spacecraft	h/km	e	i/deg	Ω/deg	ω/deg	n/deg
Observer	500	0.01	45.05	29.93	132.9	-107.74
Target	1000	0.02	45.00	94.80	199.00	-54.13

Let $\boldsymbol{x}_O = [\boldsymbol{r}_O; \boldsymbol{v}_O] = [x_O, y_O, z_O, \dot{x}_O, \dot{y}_O, \dot{z}_O]^T$ denote the orbit state of the observer spacecraft. Assume the observer observes the target using onboard optical sensors. The line-of-sight (LOS) vector from the observer to the target can be obtained by identifying points in the image and extracting the target [46,47]. In this paper, the adopted model for representing the angular measurements is given as

$$\boldsymbol{l} = [l_x, l_y, l_z]^T = \frac{\boldsymbol{r} - \boldsymbol{r}_O}{\|\boldsymbol{r} - \boldsymbol{r}_O\|} + \boldsymbol{\varepsilon}_l \in \mathbb{R}^3, \tag{67}$$

where $\boldsymbol{\varepsilon}_l \in \mathbb{R}^3$ is the measurement noise vector, $\boldsymbol{l} = [l_x, l_y, l_z]^T$ denotes the LOS vector, with l_x, l_y and l_z representing the elements along the inertial x-, y-, and z-axes, respectively.

Three cases are simulated: one standard case, one sparse observation case, and one short-arc case. The conditions of these three cases are listed in Table 2. The total navigation period of the standard case is 1800 s, with a measurement interval of 10 s. The standard case is used to test the performance of the proposed method in a general condition. In addition, the robustness of the proposed method under severe conditions is investigated using the sparse observation case and the short-arc observation case. In the sparse observation case, only 11 measurements are available, which is used to analyze whether the method is effective for conditions when information is limited. The third case has a total navigation period of 300 s, in which the performance of the method under a short observation arc is tested.

Table 2 Simulated conditions of three cases

Parameter		Standard case	Sparse observation case	Short-arc observation case
Initial covariance	Position	10^2 km^2 per axis		
	Velocity	1^2 m^2/s^2 per axis		
	Impulsive vector	5^2 m^2/s^2 per axis		
	Impulsive epoch	50^2 s^2		10^2 s^2
Standard deviation of measurement noise		1×10^{-5} per axis		
Measurement frequency		10 s	180 s	2 s
Start epoch t_0		0 s		
End epoch t_2		1800 s	1800 s	300 s
Impulsive maneuver epoch t_1		905 s	905 s	151 s

Impulsive maneuver vector	$\Delta \boldsymbol{v}_1$	$[10,10,10]^T$ m/s

Before testing the performance of the proposed method, the accuracy of the proposed modified STT in Eq. (26) and the second-order measurement model in Eq. (35) is analyzed. The standard case is employed for accuracy analysis. The process of testing the accuracy of the modified STT and the second-order measurement model is based on 1000 Monte Carlo (MC) runs. Each sample $\tilde{\boldsymbol{X}}$ is generated randomly from the normal distribution $\mathcal{N}(\tilde{\boldsymbol{X}}; \boldsymbol{X}_r, \boldsymbol{P}_X)$, with $\boldsymbol{X}_r$ being the real state listed in Table 1 and $\boldsymbol{P}_X$ being the covariance

$$\boldsymbol{P}_X = \mathrm{diag}([100^2\ \mathrm{km}^2, 100^2\ \mathrm{km}^2, 100^2\ \mathrm{km}^2, 10^2\ \mathrm{m}^2/\mathrm{s}^2, 10^2\ \mathrm{m}^2/\mathrm{s}^2, 10^2\ \mathrm{m}^2/\mathrm{s}^2, 5^2\ \mathrm{m}^2/\mathrm{s}^2, 5^2\ \mathrm{m}^2/\mathrm{s}^2, 5^2\ \mathrm{m}^2/\mathrm{s}^2, 50^2\ \mathrm{s}^2]) \tag{68}$$

For each sample $\tilde{\boldsymbol{X}}$, the true orbit state $\tilde{\boldsymbol{x}}(t)$ from t_0 to t_2 is propagated, and the state deviation $\delta \boldsymbol{x}(t)$ is obtained. Moreover, the measurement deviation $\delta \boldsymbol{z}(t)$ is calculated. The state deviation $\delta \boldsymbol{x}(t)$ and the measurement deviation $\delta \boldsymbol{z}(t)$ are also predicted using Eqs. (26) and (35), and the absolute errors (AEs) and the relative errors (REs) are obtained. The time history of the mean relative errors (MREs) of the 1000 MC runs is shown in Fig. 3. In Fig. 3, the green lines represent the impulsive maneuver epoch. The MREs of the position states are smaller than 0.35%, and the MREs of the velocity states are no larger than 6%. The position and velocity vectors have spikes in MRE around the maneuver epoch (*i.e.*, the green lines). Re-note that in Eq. (23), the residual between $\delta \boldsymbol{x}_1^*$ and $\delta \boldsymbol{x}(t_1)$ is neglected by our equations, making the accuracy of the proposed modified STT slightly degrades around the epoch t_1. However, an MRE of 6% is applicable for the modified STT to be used in orbit estimation and maneuver reconstruction.

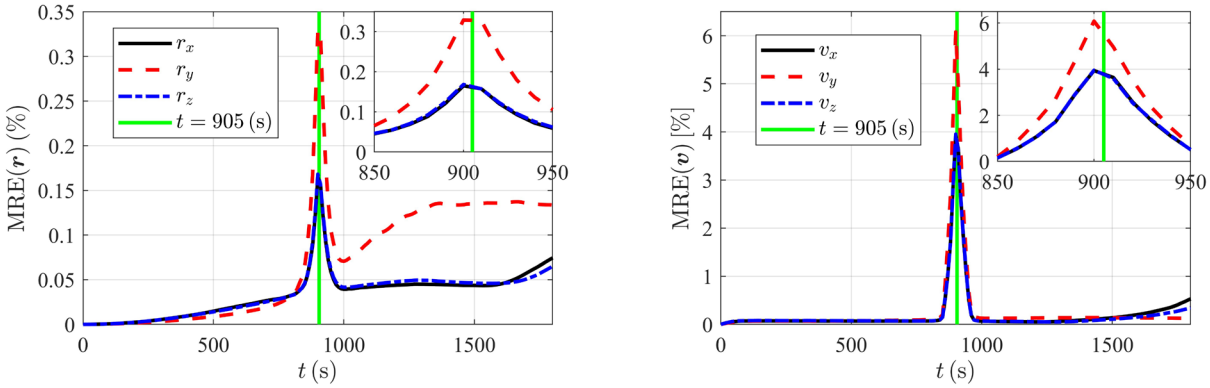

a) b)

Fig. 3 Time history of the MRE of the modified STT. a) position. b) velocity.

To better display the predicted errors of the second-order measurement model, the LOS vectors are converted to angles $\alpha(\boldsymbol{l})$ and $\beta(\boldsymbol{l})$, defined as

$$\alpha(\boldsymbol{l}) = \sin^{-1}(l_z / \|\boldsymbol{l}\|) = \sin^{-1} l_z \,, \tag{69}$$

$$\beta(\boldsymbol{l}) = \tan^{-1}(l_y / l_x) \,. \tag{70}$$

The accuracy testing results of the second-order measurement model are shown in Fig. 4. Fig. 4(a) and (b) illustrate the time history of the mean absolute error (MRE) and MRE results of 1000 MC runs. The MREs of $\alpha(\boldsymbol{l})$ and $\beta(\boldsymbol{l})$ smaller than 0.2%.

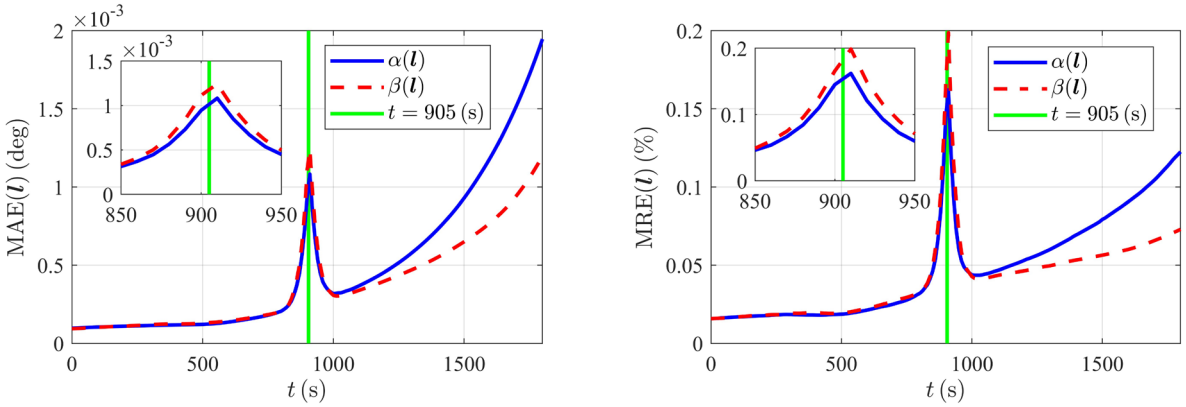

Fig. 4 Time history of the MRE of the second-order measurement model. a) MAE. b) MRE.

An independent simulation is first performed to show the convergence process of the proposed method. In the independent simulation, the position and velocity estimation errors of the initial guess are set to 10 km per axis and 1 m/s per axis, respectively. The impulsive vector estimation errors are set to be 5 m/s per axis. The impulsive epoch estimation error is given as 50 s. The STD of the LOS measurements is set to be 10^{-5} per axis (approximately 2 arcsecs). The tolerance is set as $\eta = 10^{-3}$, and the maximal iteration is set to be $i_{\max} = 10$. The algorithm converges after 5 iterations. Table 3 shows the estimated errors of each iteration. The position and velocity estimated errors are smaller than 0.23 km and 0.34 m/s, respectively. In addition, the proposed approach can provide estimations of the unknown impulsive magnitude and epoch with errors no larger than 0.3 m/s and 0.35 s, respectively.

Table 3 Estimation errors of the second-order solution in one simulation of the standard case

	Position / km			Velocity / (m/s)			Impulsive vector / (m/s)			Epoch / s
	$x(t_0)$	$y(t_0)$	$z(t_0)$	$\dot{x}(t_0)$	$\dot{y}(t_0)$	$\dot{z}(t_0)$	Δv_x	Δv_y	Δv_z	t_1
Initial guess	10	10	10	1	1	1	5	5	5	50
Iteration 1	-0.4714	-0.2973	0.0704	0.7431	-0.3589	-0.4346	-0.6602	0.8008	0.0316	8.2821
Iteration 2	-0.1981	-0.1066	0.0129	0.2929	-0.2040	-0.1040	0.0201	0.3238	-0.1968	-0.3289

Iteration 3	-0.2242	-0.1313	0.0128	0.3294	-0.1843	-0.1082	0.0228	0.2927	-0.2124	0.3388
Iteration 4	-0.2249	-0.1318	0.0129	0.3305	-0.1844	-0.1085	0.0226	0.2929	-0.2128	0.3455
Iteration 5	-0.2248	-0.1318	0.0129	0.3304	-0.1844	-0.1085	0.0226	0.2929	-0.2128	0.3457

The same independent simulation is carried out using the linear solution in Eq. (55). The linear algorithm converges using eight iterations, with the results detailed in Table 4. The position and velocity estimated errors are more than 0.3 km and 0.47 m/s, which are 1.5 times larger than those in Table 3. Additionally, the impulsive epoch errors of the linear solution (2.7603 s) are approximately one time of magnitude larger than that of the proposed second-order solution (0.3457 s).

Table 4 Estimation errors of the linear solution in one simulation of the standard case

	Position / km			Velocity / (m/s)			Impulsive vector / (m/s)			Epoch / s
	$x(t_0)$	$y(t_0)$	$z(t_0)$	$\dot{x}(t_0)$	$\dot{y}(t_0)$	$\dot{z}(t_0)$	Δv_x	Δv_y	Δv_z	t_1
Initial guess	10	10	10	1	1	1	5	5	5	50
Iteration 1	-5.8014	-4.0957	0.9770	8.9495	-3.2535	-3.7784	2.9264	3.6605	-2.8009	40.3799
Iteration 2	-1.1504	-0.8357	0.1950	1.7704	-0.4382	-0.6944	-0.1674	0.4406	-0.4714	8.7904
Iteration 3	-0.4955	-0.3501	0.0906	0.7761	-0.1350	-0.3091	-0.0425	0.2629	-0.3175	3.5572
Iteration 4	-0.4396	-0.3136	0.0794	0.6895	-0.0872	-0.2701	-0.0622	0.1965	-0.2814	3.4616
Iteration 5	-0.3156	-0.2258	0.0557	0.4969	-0.0155	-0.1859	-0.1219	0.2274	-0.2155	2.8066
Iteration 6	-0.3038	-0.2175	0.0534	0.4790	-0.0081	-0.1778	-0.1284	0.2219	-0.2088	2.7618
Iteration 7	-0.3033	-0.2171	0.0533	0.4782	-0.0078	-0.1774	-0.1287	0.2217	-0.2085	2.7604
Iteration 8	-0.3033	-0.2171	0.0533	0.4782	-0.0078	-0.1774	-0.1287	0.2216	-0.2085	2.7603

Monte Carlo simulations are further performed to investigate the estimation accuracy of the proposed algorithm. Note that the MC simulations performed herein differ from those shown in Fig. 3 and Fig. 4, as the MC simulations in Fig. 3 and Fig. 4 only examine the accuracy of the modified STT and the second-order measurement model. The state estimated errors of the 100 MC runs (using the second-order solution) of the standard case are shown in Fig. 5. It should be noted that the proposed method can only estimate $\boldsymbol{x}_0$, $\Delta\boldsymbol{v}_1$ and t_1. The state estimated errors (*i.e.*, the blue lines) in Fig. 5 are obtained by propagating the estimations ($\boldsymbol{x}_0$, $\Delta\boldsymbol{v}_1$ and t_1) and then comparing them with the true orbits. Moreover, the 3-STD (3σ) bounds of the estimated errors, which are calculated numerically using these MC points, are presented by the solid red lines. The position and velocity estimated errors of the 100 MC runs are smaller than 0.75 km and 1.2 m/s, respectively. The distributions of the estimations of $\Delta\boldsymbol{v}_1$ and t_1 using the second-order solution are presented in Fig. 6. In Fig. 6, the blue and red boxes represent the results of the second-order and linear solutions, respectively, and the circles represent the outliers. Using the second-order solution, the absolute errors of estimations of the impulsive epoch t_1 are no larger than 4 s. The estimation errors of the impulsive vector $\Delta\boldsymbol{v}_1$ are less than 0.5 m/s per axis. Additionally, the results of the linear solution are shown in Fig. 6 as a

comparison. As shown in Fig. 6, the distributions of the red boxes are larger than those of the blue boxes, indicating that the linear solution has a poor maneuver reconstruction performance.

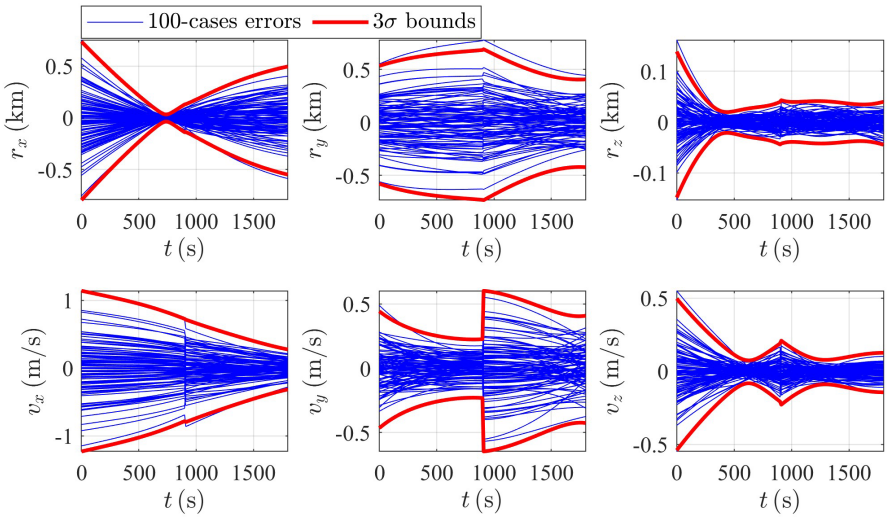

Fig. 5 Monte Carlo simulation results of the proposed method in the standard case.

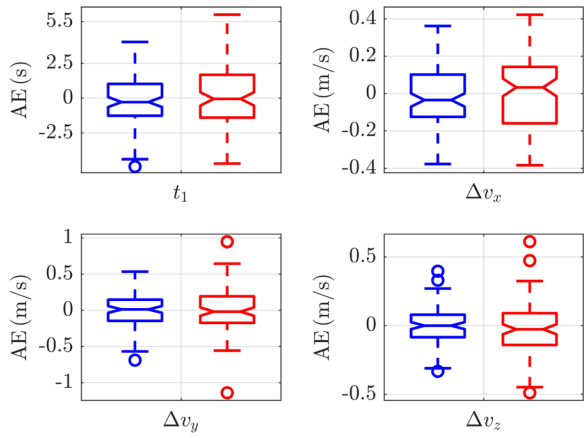

Fig. 6 Estimated error distributions of the impulsive vector and impulsive epoch in the standard case.

To investigate the uncertainty quantification (UQ) capacities of the proposed method, the Mahalanobis distances (MD) are calculated in the MC simulations. The MD is defined as

$$\mathrm{MD} = \sqrt{(\hat{\boldsymbol{X}} - \boldsymbol{X}_r)^T \hat{\boldsymbol{P}}^{-1} (\hat{\boldsymbol{X}} - \boldsymbol{X}_r)}, \tag{71}$$

where $\hat{\boldsymbol{X}}$ and $\boldsymbol{X}_r$ are the estimated and true parameter vector (including the initial orbit state, and impulsive maneuver epoch and vector), respectively, and $\hat{\boldsymbol{P}}$ is the covariance matrix predicted by the algorithm. As shown in Eq. (71), $\mathrm{MD} = \sqrt{n_X}$ ($n_X = 10$ is the dimension of the parameter vector $\boldsymbol{X}_r$) indicates that the estimated error

$\hat{\boldsymbol{X}} - \boldsymbol{X}_r$ lies on the 1σ boundary of the covariance $\hat{\boldsymbol{P}}$, whereas $\mathrm{MD} = 3\sqrt{n_X}$ means that the estimated error lies on the 3σ boundary of the covariance. The MD results of the second-order and linear solutions are plotted in Fig. 7. In Fig. 7, the blue and red boxes represent the MD results of the second-order and linear solutions, respectively, and the circles represent the outliers. Both two solutions have MDs smaller than $3\sqrt{n_X}$, and the true estimated errors are inside the 3σ ellipsoid of the covariance predicted by the algorithm. This means that the proposed algorithm (Eq. (66)) can effectively quantify the estimated uncertainties. Additionally, the linear solution has larger MD values, showing that its UQ capacity is poorer than that of the second-order solution [36]. Thus, one can see from Table 4, Fig. 6, and Fig. 7 that the second-order solution outperforms the linear version in terms of convergence, accuracy, and uncertainty quantification capacity. In the following of this paper, the second-order solution is employed.

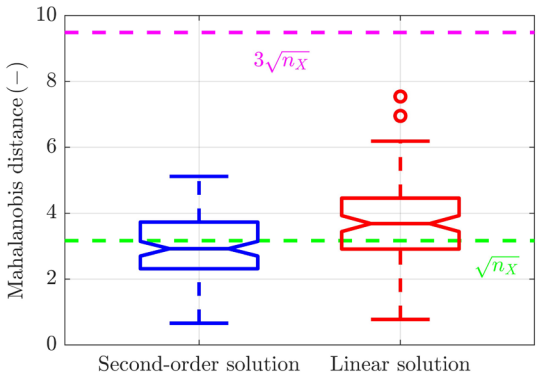

Fig. 7 Mahalanobis distance results of the MC simulation.

To better investigate the performance of the proposed method, comparison simulations are performed: the extended Kalman filter (EKF) [48], the adaptive extended Kalman filter (AEKF) [9], the thrust-Fourier-coefficient based extended Kalman filter (TFC-EKF) [7,14] and the TFC-EKF with an LSM smoother (TFC-EKF-Smoother). The EKF is the basic method without any improvement to handle unknown maneuvers, the AEKF belongs to the OD reinitiation method, and the TFC-EKF pertains to filtering-through approaches. Additionally, the TFC-EKF-Smoother belongs to the batch method. In the TFC-EKF-Smoother, upon the impulse maneuver is detected by the TFC-EKF, pre- and post-maneuver ODs are performed using the LSM. The standard case is simulated, and 100 MC runs are performed for each method. The metric used to evaluate the performance of different methods is the root mean square error (RMSE). The RMSE results of the 100 MC runs of the different methods are shown in Table 5 and Fig. 8. The RMSE results of the proposed methods are labeled 'STT-LSM' as the modified STT is proposed based on the STT technique and the second-order optimal solution is extended from the LSM. The AEKF and TFC-

EKF perform better than the standard EKF method but are much worse than the proposed method. The RMSEs of the proposed STT-LSM are at least one order of magnitude less than those of the TFC-EKF. By adding an LSM smoother to the TFC-EKF, the estimated errors are significantly reduced. However, the estimated errors of the TFC-EKF-Smoother are still larger than those of the proposed method. It is because the TFC-EKF-Smoother estimates the pre- and post-maneuver orbits independently, whereas the proposed method uses both pre- and post-maneuver measurements. In addition, the performance of the LSM smoother can also be impacted by the maneuver detection errors of the TFC-EKF.

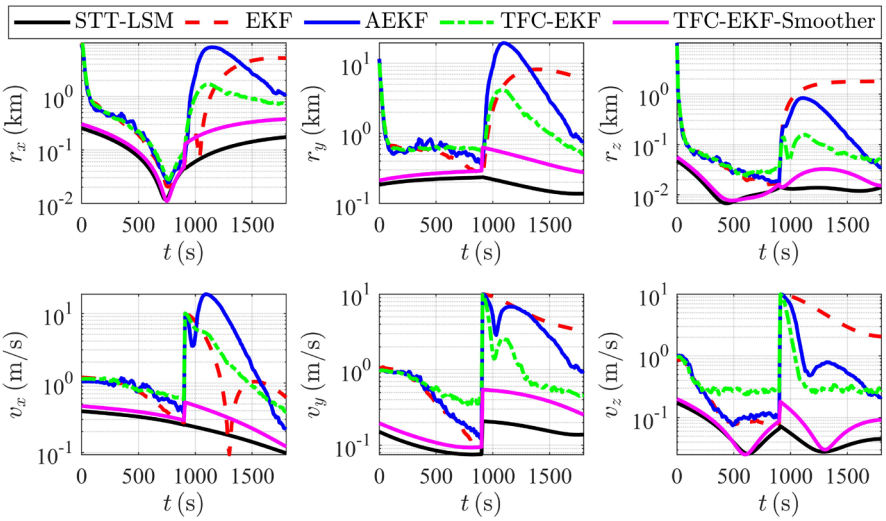

Fig. 8 Time history of the RMSEs of different methods in the standard case.

Table 5 RMSE results of different methods in the standard case

Method	Position RMSE / km			Velocity RMSE / (m/s)		
	x	*y*	*z*	*x*	*y*	*z*
STT-LSM	0.1111	0.1942	0.0142	0.2499	0.1329	0.0568
EKF	1.8178	3.4492	0.8160	1.6217	3.1456	2.5982
AEKF	2.2430	4.0539	0.2580	3.6178	2.3817	0.9778
TFC-EKF	0.8198	1.3074	0.1275	1.7901	1.0748	0.6871
TFC-EKF-Smoother	0.2035	0.3424	0.0211	0.3438	0.2721	0.0803

One of the main purposes of the proposed method is to accurately reconstruct the unknown impulsive maneuver. The maneuver reconstruction performance of the proposed method is compared with the other four competitive methods based on 100 MC runs. To better virtualize the results, the impulsive maneuver $\Delta\boldsymbol{v}_1$ is represented using four parameters: the time t_1, magnitude $\|\Delta\boldsymbol{v}_1\|$, declination $\alpha(\Delta\boldsymbol{v}_1)=\sin^{-1}(\Delta v_z/\|\Delta\boldsymbol{v}_1\|)$, and right ascension $\beta(\Delta\boldsymbol{v})=\tan^{-1}(\Delta v_y/\Delta v_x)$. The two angles $\alpha(\Delta\boldsymbol{v}_1)$ and $\beta(\Delta\boldsymbol{v}_1)$ are used to describe the direction of the impulsive maneuver in the ECEI coordinate. Following [27], the methods for reconstructing the impulsive maneuver based on

the estimations of the EKF, AEKF, TFC-EKF, and TFC-EKF-Smoother are given as follows. First, the orbit estimation at the initial epoch t_0 is propagated forward, and the orbit estimation at the final epoch t_2 is propagated backward. Then, the time when the two orbits cross or come closest together (with minimum separation distance) is determined as the estimated time of the impulsive maneuver t_1. The estimated time of the impulsive maneuver t_1 is obtained as

$$t_1 = \arg\min \left\| \boldsymbol{r}_{\text{pre}}(t) - \boldsymbol{r}_{\text{post}}(t) \right\|, \tag{72}$$

and the estimated impulsive is expressed as

$$\Delta \boldsymbol{v}_1 = \boldsymbol{v}_{\text{post}}(t_1) - \boldsymbol{v}_{\text{pre}}(t_1). \tag{73}$$

where $\boldsymbol{x}_{\text{pre}}(t) = [\boldsymbol{r}_{\text{pre}}(t); \boldsymbol{v}_{\text{pre}}(t)]$ and $\boldsymbol{x}_{\text{post}}(t) = [\boldsymbol{r}_{\text{post}}(t); \boldsymbol{v}_{\text{post}}(t)]$ are the pre- and post-maneuver orbit, respectively.

The maneuver reconstruction results of the 100 MC runs are presented in Fig. 9, alongside zoomed in plots around the true values to clearly show the results obtained by the proposed method. In Fig. 9, the blue square represents the true value, and the results of the STT-LSM, the EKF, the AEKF, the TFC-EKF, and the TFC-EKF-Smoother are colored black, red, blue, green, and magenta, respectively. Fig. 9 (a) shows the projections of the time t_1 and the magnitude $\left\| \Delta \boldsymbol{v}_1 \right\|$, and Fig. 9 (b) shows the projections of the two angles $\alpha(\Delta \boldsymbol{v}_1)$ and $\beta(\Delta \boldsymbol{v}_1)$. The blue square depicts the real parameters of the impulsive maneuver. The estimations using the proposed method, the EKF, the AEKF, the TFC-EKF, and the TFC-EKF-Smoother are shown by the black crosses, red squares, blue diamonds, green circles, and magenta triangles, respectively. Moreover, the 3σ bounds (obtained from the MC distributions) of the estimations are shown using the dashed lines with the corresponding colors. The detailed mean values and the STD of the maneuver reconstruction errors of 100 MC runs using different methods are listed in Table 6.

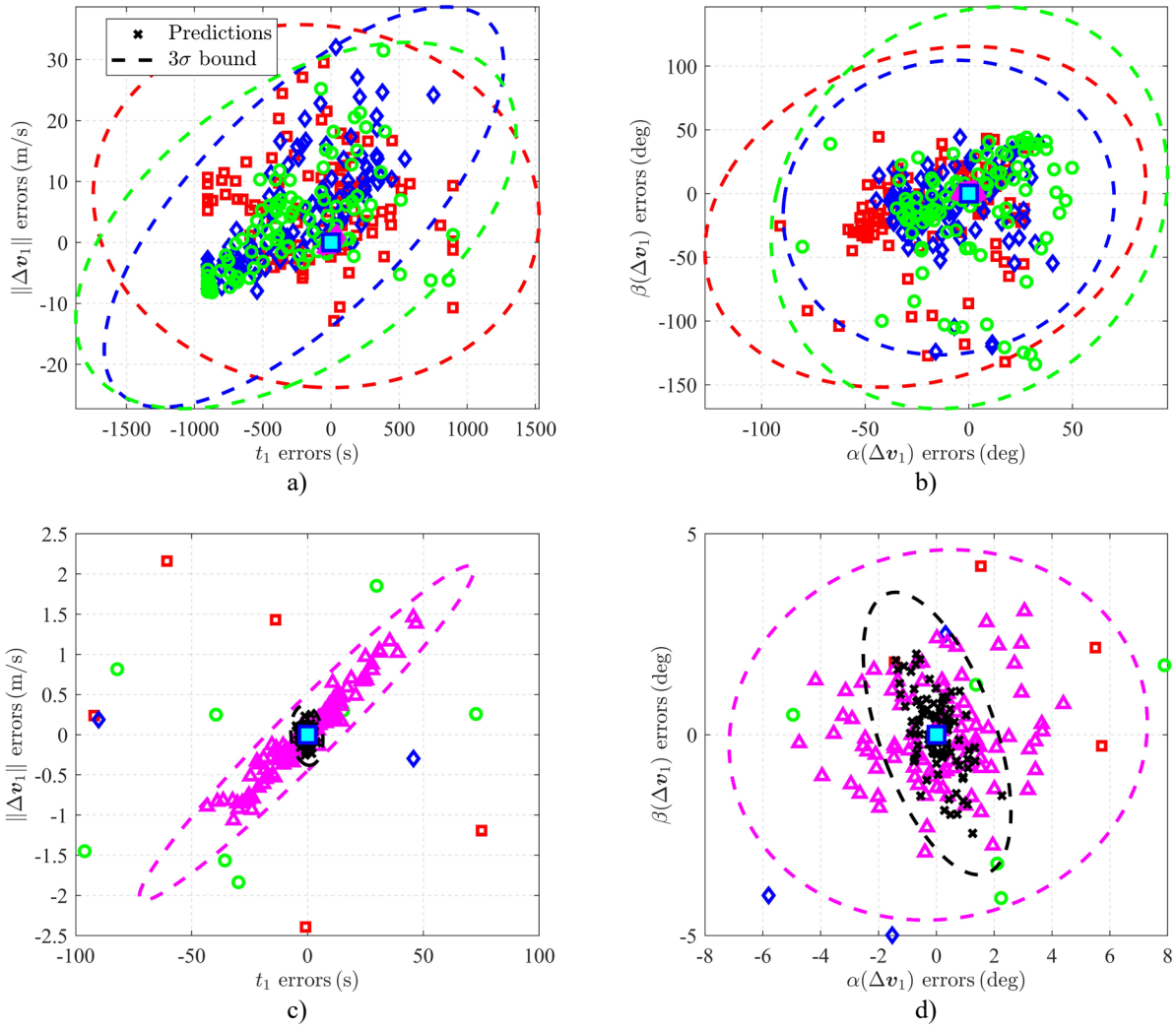

Fig. 9 Maneuver reconstruction results of different methods in the standard case. a) Projections of time t_1 and magnitude $\|\Delta v_1\|$. b) Projections of directions $\alpha(\Delta v_1)$ and $\beta(\Delta v_1)$. c) Larger plot of a). d) Larger plot of b).

Table 6 Maneuver reconstruction results in the standard case

		t_1 / s	$\|\Delta v_1\|$ / (m/s)	$\alpha(\Delta v_1)$ / deg	$\beta(\Delta v_1)$ / deg
STT-LSM	Mean error	-0.2589	-0.00859	0.0265	0.0281
	STD	1.8367	0.0992	0.6783	0.9341
EKF	Mean error	-107.75822	5.9618	-20.9953	-18.2323
	STD	434.6810	7.9098	28.2661	35.5231
AEKF	Mean error	-198.3669	5.8019	-9.7565	-11.0394
	STD	389.3845	8.7222	21.2337	30.7164
TFC-EKF	Mean error	-257.6306	2.7789	0.2638	-11.2264
	STD	429.0699	7.9837	25.4283	41.8890
TFC-EKF-Smoother	Mean error	-0.3562	0.0198	0.0644	-0.0057
	STD	19.1759	0.5534	1.9219	1.2253

Fig. 9 and Table 6 show that the magnitude of the maneuver reconstruction errors of the proposed method are typically two orders of magnitude smaller than those of the EKF, AEKF, and TFC-EKF. The predicted times of the

impulsive maneuver using the EKF, AEKF, and TFC-EKF seriously deviate from the true value. This is because these filters cannot accurately estimate the spacecraft orbit, especially the segments close to the maneuver. In turn, the time when the pre- and post-maneuver orbits are crossed may be distorted by the position estimated uncertainty [27]. In addition, although an LSM smoother can significantly improve the maneuver reconstruction accuracy, the reconstruction errors of the TFC-EKF-Smoother are more than one order of magnitude larger than those of the proposed method.

To investigate the computational cost of the proposed method, the time of the 100 MC runs is recorded. Fig. 10 illustrates the distributions of the time cost of 100 MC runs of different methods. The histogram represents the mean time cost. The lower and upper bounds of the error bar denote the minimal and maximal computational times, respectively. The detailed mean, minimal, and maximal time costs are listed in Table 7. The EKF and AEKF have similar time costs, which are lower than 0.2 s. The mean time costs of the proposed method and TFC-EKF-Smoother are 3.6524 s and 1.0982 s. The proposed method has the highest time consumption, which is 18 times as much as the EKF costs and 3.6 times as much as the TFC-EKF-Smoother costs. Note that the proposed method is a postprocessing method that determines the spacecraft orbit using both pre- and post-maneuver measurements. Moreover, the proposed method calculates second-order terms, whereas the TFC-EKF-Smoother only computes linear terms. Therefore, it is reasonable that the proposed method has the best accuracy and a higher computational cost. However, the computational time is relatively small compared with the whole navigation period. Therefore, the proposed method remains applicable for real-time use. The above simulations are performed using MATLAB R2022a on a personal computer with a 2.5 GHz processor (12th Gen Intel(R) Core(TM) i5-12500H) and 16 GB RAM.

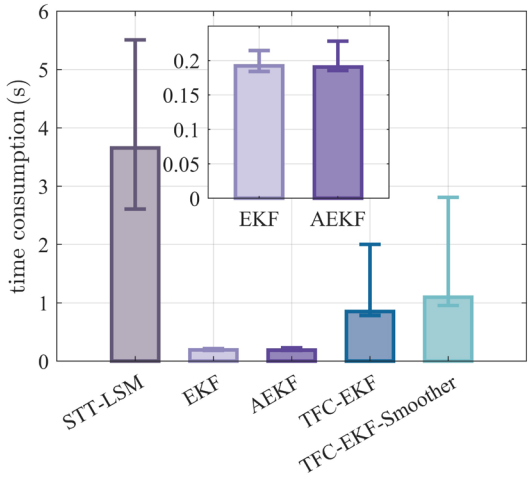

Fig. 10 Distribution of the time consumption of different methods.

Table 7 Mean, maximal, and minimal of different methods

Method	Mean run time / s	Maximal run time / s	Minimal run time / s
STT-LSM	3.6524	5.5091	2.6073
EKF	0.1920	0.2143	0.1840
AEKF	0.1904	0.2281	0.1852
TFC-EKF	0.8531	2.0004	0.7853
TFC-EKF-Smoother	1.0982	2.8082	0.9539

The proposed method and four other competitive methods are used to solve the OD problem of the sparse observation case. The conditions of the sparse observation case are listed in Table 2. Monte Carlo simulations with 100 runs are performed for the five methods, with the maneuver reconstruction results shown in Table 8. Compared with the standard case, the maneuver reconstruction accuracy of the proposed method degrades in the sparse case. However, the proposed method still outperforms the other four methods, with maneuver reconstruction errors at least one order of magnitude less than those of the TFC-EKF-Smoother.

Table 8 Maneuver reconstruction results in the sparse observation case

		t_1 / s	$\|\Delta \boldsymbol{v}_1\|$ / (m/s)	$\alpha(\Delta \boldsymbol{v}_1)$ / deg	$\beta(\Delta \boldsymbol{v}_1)$ / deg
STT-LSM	Mean error	0.4188	0.0237	0.1643	-0.6248
	STD	7.5933	0.3661	2.1781	3.3343
EKF	Mean error	-74.7257	5.5660	-17.7931	-14.3302
	STD	326.4619	7.73082	25.2547	36.4788
AEKF	Mean error	-69.2292	10.4335	-18.2300	-8.2055
	STD	383.0920	8.3188	28.4933	33.6777
TFC-EKF	Mean error	-339.9047	1.2827	5.7918	-30.2353
	STD	390.4735	7.0658	21.4907	56.4150
TFC-EKF-Smoother	Mean error	3.9087	0.2467	3.0784	-0.1293
	STD	87.7816	2.7239	11.9606	6.7121

Finally, the performance of the proposed method in handling short-arc observations is validated via comparing it with the EKF, AEKF, TFC-EKF, and TFC-EKF-Smoother. The maneuver reconstruction results of the MC

simulations are shown in Table 9. In the short-arc observation case, the performance of the TFC-EKF-Smoother degrades seriously as only 2.5 minutes of measurements are available for the TFC-EKF-Smoother to estimate the pre- and post-maneuver orbits. However, the proposed method can make full use of all measurements, and thus, its maneuver reconstruction errors are much smaller. Compared with the standard case, the t_1 estimated STD of the proposed method increases from 1.8367 s to 2.3514 s, and the $\|\Delta \boldsymbol{v}_1\|$ estimated STD of the proposed method increases from 0.0992 m/s to 2.455 m/s. The measurement interval impacts the reconstruction performance of the proposed method, which will be discussed in Sec. IV.B.3 in detail.

Table 9 Maneuver reconstruction results in the short-arc observation case

		t_1 / s	$\|\Delta \boldsymbol{v}_1\|$ / (m/s)	$\alpha(\Delta \boldsymbol{v}_1)$ / deg	$\beta(\Delta \boldsymbol{v}_1)$ / deg
STT-LSM	Mean error	0.1245	0.1772	0.6833	0.8030
	STD	2.3514	2.4550	8.3861	4.7656
EKF	Mean error	41.2572	-3.1996	-8.6799	-60.8419
	STD	130.5298	2.7911	17.1934	16.0249
AEKF	Mean error	127.8097	33.5385	-26.8495	-52.2776
	STD	59.3794	15.7191	9.9017	11.4083
TFC-EKF	Mean error	55.1615	6.8669	-13.6974	-50.0177
	STD	127.6545	5.6651	13.0772	8.8832
TFC-EKF-Smoother	Mean error	35.7830	8.5508	-6.8496	-37.6454
	STD	129.7907	9.0153	10.4966	47.3876

2. GEO testing case

One LEO testing case is not thorough enough to analyze the performance of the proposed method, and a GEO testing case is added herein. A target entering a GEO from a geostationary transfer orbit (GTO) and an observer moving on a GTO are considered in this example, with their orbit parameters listed in Table 10. An impulsive maneuver, with a magnitude of approximately 1.4773 km/s, is executed by the target to enter the GEO at the epoch $t_1 = 10830$ s. The measurement interval is set as 60 s. Note that the intent of this example is to demonstrate the proposed method's capacity for accurately estimating the orbit and reconstructing the unknown impulsive maneuver for a GEO spacecraft. In practice, an impulsive assumption is poor when the magnitude is on the order of 1 km/s. In this case, continuous maneuver assumption is actually more true-to-life, and methods like the OCBE [31], minimum model error estimation (MME) [49], and TFC-EKF [7] may be more effective.

Table 10 Nominal orbit elements of the target and the observer in the GEO testing case

Spacecraft	Orbit type	h / km	e	i / deg	Ω / deg	ω / deg	n / deg
Observer	GTO ($t_0 = 0$ s)	17993.0215	0.7301	0	0	0	180
	GEO ($t_1 = 10830$ s)	35786.0816	0	0	0	0	0

Target	GTO ($t_0 = 0$ s)	17993.0215	0.7301	0	0	0	170

The proposed method and the four competitive methods are employed to resolve the OD problem in this GEO testing case. The initial estimated errors, the tolerance, and the maximal iteration of the proposed method are set the same as those in the LEO testing case. One hundred MC runs are performed for each method, with the averaged RMSEs provided in Table 11 and the maneuver reconstruction results shown in Fig. 11 and Table 12. In Fig. 11, the blue square represents the true value, and the results of the STT-LSM and the TFC-EKF-Smoother are colored black and magenta, respectively. The maneuver construction results of the EKF, AEKF, and TFC-EKF are not plotted in Fig. 11, as their estimations seriously deviate from the true values. The state estimated RMSEs and the maneuver reconstruction errors of the proposed method are half of those of the TFC-EKF-Smoother and are one-thousandth of those of the EKF, AEKF, and TFC-EKF.

Table 11 RMSE results of different methods in the GEO testing case

Method	Position RMSE / km			Velocity RMSE / (m/s)		
	x	y	z	x	y	z
STT-LSM	0.3966	0.6584	0.0110	0.0713	0.0549	0.0022
EKF	1515.1264	5739.9999	0.0483	269.9595	614.3749	0.0324
AEKF	1712.6599	6978.8532	0.0468	444.0001	596.6479	0.0466
TFC-EKF	571.4159	2478.5652	0.1055	158.7369	265.6733	0.6964
TFC-EKF-Smoother	0.6361	1.2656	0.0125	0.1214	0.0989	0.0027

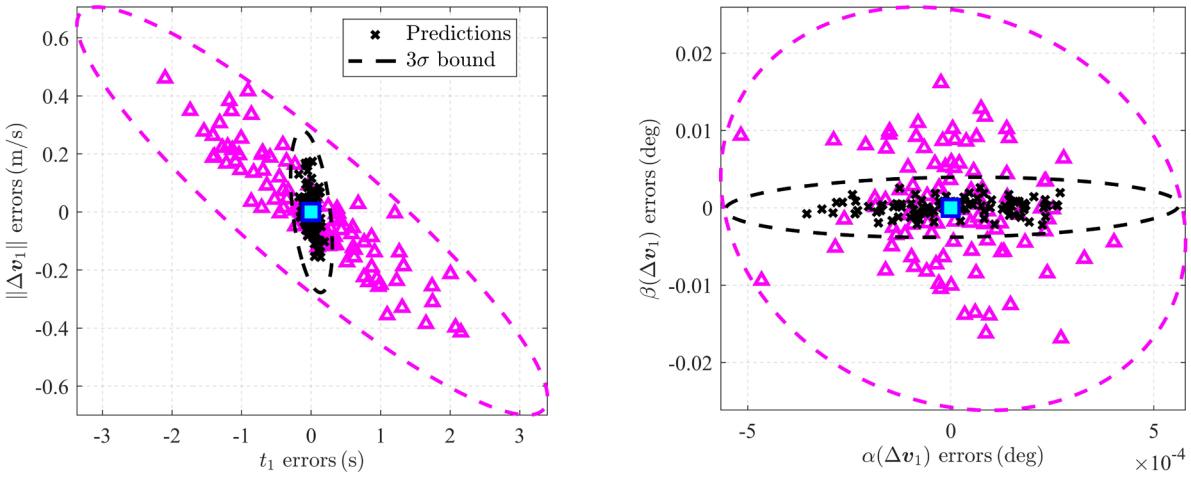

a) b)

Fig. 11 Maneuver reconstruction results in the GEO testing case. a) Projections of time t_1 and magnitude $\|\Delta v_1\|$. b) Projections of directions $\alpha(\Delta v_1)$ and $\beta(\Delta v_1)$.

Table 12 Maneuver reconstruction results in the GEO testing case

	t_1 / s	$\|\Delta v_1\|$ / (m/s)	$\alpha(\Delta v_1)$ / deg	$\beta(\Delta v_1)$ / deg

STT-LSM	Mean error	0.0058	0.0012	3.2463e-6	7.1319e-5
	STD	0.0796	0.0741	1.4851e-4	1.0335e-3
EKF	Mean error	2542.7791	-476.3840	-0.0041	-87.8977
	STD	47.9845	3.32307	0.0552	0.1422
AEKF	Mean error	2248.1761	-466.6020	-0.0021	-89.9403
	STD	48.8883	3.4697	0.0537	0.1478
TFC-EKF	Mean error	2006.46444	-263.2457	0.0036	-15.7540
	STD	586.0104	62.9861	0.0576	4.8190
TFC-EKF-Smoother	Mean error	0.01617	0.0029	5.8849e-6	-1.1871e-4
	STD	0.8991	0.1868	1.5210e-3	0.0069

It also should be noted that, compared with the LEO testing case, the proposed method has a better maneuver reconstruction performance when applied to the GEO testing case. The STD of the estimated errors of t_1 in the GEO testing case is less than 0.1 s, whereas, in the LEO testing case, it is approximately 2 s. This performance improvement mainly owes to the fact that the GEO testing case has a larger impulsive maneuver. A larger impulsive maneuver changes the orbits more obviously, and in turn, it is easier to reconstruct the maneuver from the measurements. On the contrary, if the impulsive maneuver is very small, its impacts on the orbit can be absorbed by the measurement noise, making it difficult to be reconstructed. The effects of the magnitudes of the impulsive maneuver will be discussed in Sec. IV.B.2.

B. Sensitivity analysis

1. Sensitivity to the initial guess

The proposed method requires an initial estimation of $\Delta\boldsymbol{v}_1$ and t_1. In this subsection, an analysis of the sensitivity of the method to the accuracy of initial estimations $\Delta\boldsymbol{v}_1^{(0)}$ and $t_1^{(0)}$ is presented. The standard case in the LEO testing case is taken as the simulated example. First, we investigate the effects of the accuracy of $t_1^{(0)}$ on the method's performance. The initial estimation $t_1^{(0)}$ can come from maneuver detections. We traverse $t_1^{(0)}$ from the initial epoch t_0 to the end epoch t_2, with an interval of 50 s. For each $t_1^{(0)}$, the direction of estimation $\Delta\boldsymbol{v}_1^{(0)}$ is randomly generated, and the magnitude of estimation $\Delta\boldsymbol{v}_1^{(0)}$ is fixed as $\left\|\Delta\boldsymbol{v}_1^{(0)}\right\| = 30\sqrt{3}$ m/s, which is three times of the true value. Monte Carlo simulation with 100 runs is carried out for each $t_1^{(0)}$. One run of the Monte Carlo simulation is considered a successful computation if the following conditions are satisfied: the position and velocity estimated errors along any axis are smaller than 1 km and 1 m/s, respectively; the algorithm converges in 10 iterations.

For each $t_1^{(0)}$, the convergence ratio (CR) is defined as

$$\mathrm{CR}=\frac{N_{\text{successful computation}}}{100}\times 100\%\,, \tag{74}$$

where $N_{\text{successful computation}}$ is the number of successful runs. The CR and the average number of iterations with respect to the initial estimation of the impulsive maneuver epoch are shown in Fig. 12(a). In Fig. 12(a), the blue rectangle represents the feasible range (*i.e.*, CR is 100%), and the red dashed line denotes the true value. The results when $t_1^{(0)}<600$ s are not displayed as the proposed method fails to converge in all MC runs. When $t_1^{(0)}$ has an error of no more than 500 s, the convergence ratio is 100%. The CR degrades when the error of $t_1^{(0)}$ is larger than 600 s or is smaller than -150 s. The length of 750 s is large compared with the total navigation period (1800 s), which is not a harsh requirement to satisfy. Moreover, it is found that the method needs more iterations as the absolute error of $t_1^{(0)}$ increases. When the error of $t_1^{(0)}$ is 50 s, 5 iterations are used, while more than 7 iterations are required when the error of $t_1^{(0)}$ is 600 s. Compared with the condition when $t_1^{(0)}>t_1$, the convergence properties under the condition $t_1^{(0)}<t_1$ are poorer. It is because when the initial guess of the maneuver epoch is anterior to when it actually is, there exists a gap between the virtual state and the true state (as shown in Fig. 1(b)), making the developed modified STT slightly inaccurate around the maneuver epoch. However, the nonconvergence under this condition is innocuous for the method, as in a true-to-life, a maneuver will likely always be detected after it is executed.

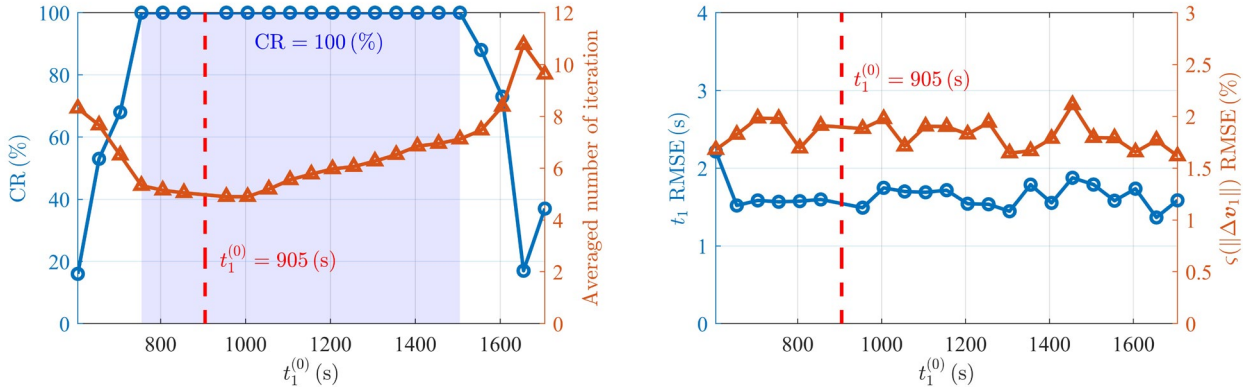

Fig. 12 Performance of the proposed method under different initial estimations of t_1. a) Convergence. b) Maneuver reconstruction performance.

In addition, the maneuver reconstruction performances of the proposed method under different $t_1^{(0)}$ are shown in Fig. 12(b). In Fig. 12(b), $\varsigma(\|\Delta \boldsymbol{v}_1\|)=\|\Delta \boldsymbol{v}_1-\Delta \hat{\boldsymbol{v}}_1\|/\|\Delta \boldsymbol{v}_1\|\times 100\%$ represents the relative error of the impulsive maneuver vector. The nonconvergence runs are removed when computing the RMSEs of t_1 and $\varsigma(\|\Delta \boldsymbol{v}_1\|)$. As is shown in Fig.

12(b), the initial guess of t_1 will not influence the maneuver reconstruction performance provided that the proposed algorithm can converge.

Then, MC simulations are implemented for different $\left\|\Delta\boldsymbol{v}_1^{(0)}\right\|$. For each $\left\|\Delta\boldsymbol{v}_1^{(0)}\right\|$, the initial estimation of the impulsive maneuver epoch is set to be $t_1^{(0)} = t_1 + 300$ s. The results are presented in Fig. 13. For any given $\left\|\Delta\boldsymbol{v}_1^{(0)}\right\|$, the convergence ratio is 100%, and the average number of iterations is no more than 7. The proposed method can converge even when $\left\|\Delta\boldsymbol{v}_1^{(0)}\right\|$ is 10 times larger than the true value. The initial guess of the maneuver magnitude does not impact the maneuver reconstruction performance.

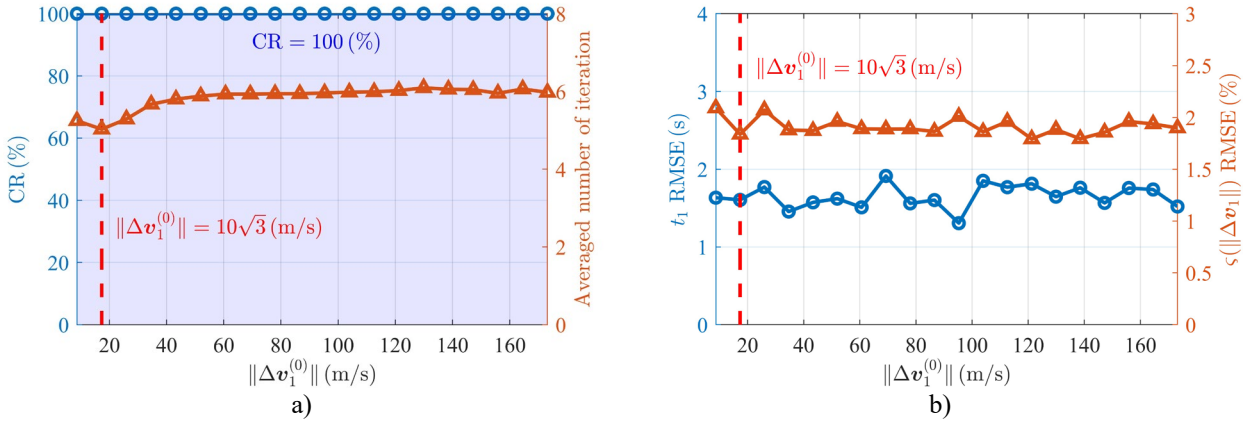

Fig. 13 Performance of the proposed method under different initial estimations of $\left\|\Delta\boldsymbol{v}_1\right\|$. a) Convergence. b) Maneuver reconstruction performance.

2. Sensitivity to the magnitude of the impulsive maneuver

Influences of the maneuver magnitude on the convergence and maneuver reconstruction performance are demonstrated in Fig. 14. The true impulsive maneuver is given as $\lambda\Delta\boldsymbol{v}_1$, where λ is a scaling factor. For each given λ, the initial guesses are given as $t_1^{(0)} = t_1 + 300$ s and $\left\|\Delta\boldsymbol{v}_1^{(0)}\right\| = 3\lambda\left\|\Delta\boldsymbol{v}_1\right\|$. As shown in Fig. 14(a), the proposed method requires more iterations when the maneuver magnitude is smaller. It fails to converge in some runs when $\lambda < 1$. However, these runs are judged as 'nonconvergence' as the proposed method fails to converge in ten iterations rather than it diverges. Additionally, one can see from Fig. 14(b) that the maneuver reconstruction performance is better when the maneuver magnitude is larger. The reconstruction relative errors are lower than 0.2% when the impulsive maneuver is 100 m/s per axis, whereas the relative errors are larger than 20% when the impulsive maneuver is 1 m/s per axis. Smaller maneuvers will more likely be absorbed by the measurement noises.

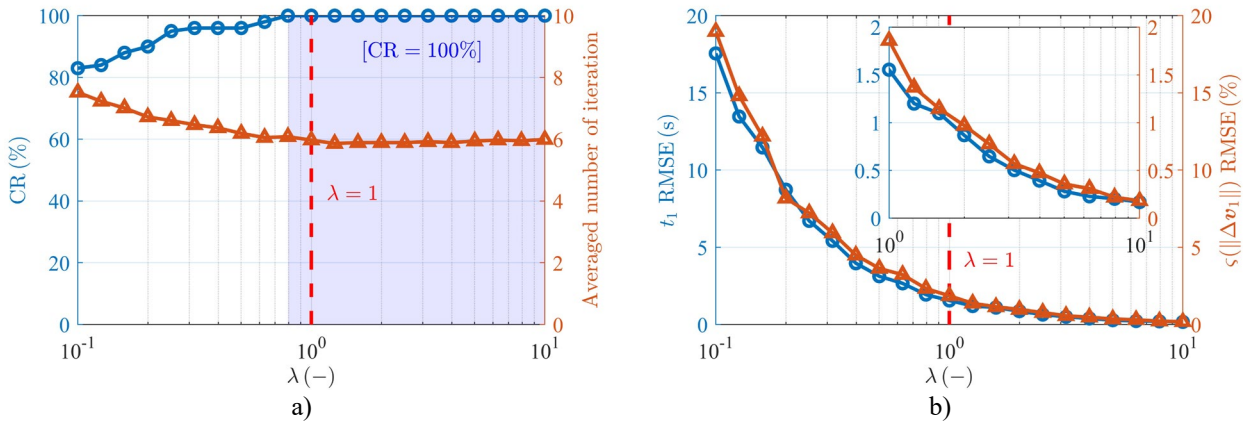

Fig. 14 Performance of the proposed method under different maneuver magnitude. a) Convergence. b) Maneuver reconstruction performance.

3. Sensitivity to the measurement interval

The convergence and maneuver reconstruction performance of the proposed method under different measurement intervals are presented in Fig. 15. The proposed method converges in all runs. The required number of iterations increases, and the maneuver reconstruction performance degrades as the measurement interval dt increases. When $dt = 1$ s, the time estimation RMSE is approximately 0.5 s, whereas the time estimation errors are larger than 8 s when $dt = 180$ s. Shortening measurement intervals and adding more measurements can improve maneuver reconstruction accuracy.

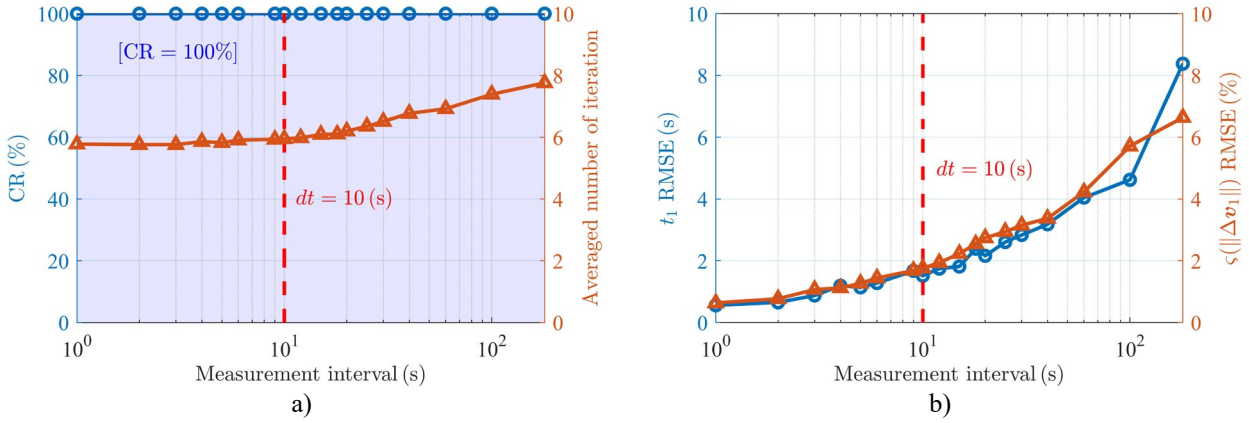

Fig. 15 Performance of the proposed method under different measurement intervals. a) Convergence. b) Maneuver reconstruction performance.

V. Conclusion

The proposed method can accurately estimate the orbit and can precisely and directly reconstruct the direction, magnitude, and epoch of an impulsive maneuver during the orbit determination process. The core of the proposed method is the modified state transition tensor (STT) for directly propagating the orbit under impulsive maneuver

uncertainties. Accuracy analysis indicates that the modified STT has a relative error of no more than 6%. Monte Carlo simulations show that using the proposed method, convergence is achieved in a few iterations (no more than seven). The maneuver reconstruction errors of the proposed method are at least one order of magnitude less than those of the competitive methods. The time consumption of the proposed method is higher than that of the conventional extended Kalman filter but is still applicable for real-time use. The proposed method can effectively handle severe cases such as sparse or short-arc observations, with estimated errors of less than 10% of competitive methods. Sensitivity analysis shows that the proposed method does not rely on accurate maneuver detection and can converge even when the initial guess is 10 times larger than the true value. In addition, increasing maneuver magnitude and shortening measurement interval can improve the maneuver reconstruction performance of the proposed method.

Acknowledgments

This research was funded by the National Natural Science Foundation of China (grant number 51827806) and the Basic Scientific Research Project (grant number JCKY2020903B002). The authors also thank Dr. Xiangyu Li and Dr. Tong Qin for the helpful discussion.

References

[1] Kim, Y., and Park, S. Y. “Perturbative Analysis on Orbital Kinematics of Flybys and Applications to Doppler Observation.” *Journal of Guidance, Control, and Dynamics*, Vol. 38, No. 9, 2015, pp. 1690–1698. https://doi.org/10.2514/1.G000979.

[2] Xiong, K., Zhang, H. Y., and Chan, C. W. “Performance Evaluation of UKF-Based Nonlinear Filtering.” *Automatica*, Vol. 42, No. 2, 2006, pp. 261–270. https://doi.org/https://doi.org/10.1016/j.automatica.2005.10.004.

[3] Kalman, R. E. “A New Approach to Linear Filtering and Prediction Problems.” *Journal of Fluids Engineering, Transactions of the ASME*, Vol. 82, No. 1, 1960, pp. 35–45. https://doi.org/10.1115/1.3662552.

[4] Adurthi, N., and Singla, P. “Conjugate Unscented Transformation-Based Approach for Accurate Conjunction Analysis.” *Journal of Guidance, Control, and Dynamics*, Vol. 38, No. 9, 2015, pp. 1642–1658. https://doi.org/10.2514/1.G001027.

[5] Nastasi, K. M., and Black, J. T. “Adaptively Tracking Maneuvering Spacecraft with a Globally Distributed, Diversely Populated Surveillance Network.” *Journal of Guidance, Control, and Dynamics*, Vol. 42, No. 5, 2019, pp. 1033–1048. https://doi.org/10.2514/1.G003743.

[6] Zhou, X., Qin, T., and Meng, L. "Maneuvering Spacecraft Orbit Determination Using Polynomial Representation." *Aerospace*, Vol. 9, No. 5, 2022, p. 257. https://doi.org/10.3390/aerospace9050257.

[7] Ko, H. C., and Scheeres, D. J. "Tracking Maneuvering Satellite Using Thrust-Fourier-Coefficient Event Representation." *Journal of Guidance, Control, and Dynamics*, Vol. 39, No. 11, 2016, pp. 2554–2562. https://doi.org/10.2514/1.G000353.

[8] Jiang, Y., Ma, P., and Baoyin, H. "Residual-Normalized Strong Tracking Filter for Tracking a Noncooperative Maneuvering Spacecraft." *Journal of Guidance, Control, and Dynamics*, Vol. 42, No. 10, 2019, pp. 2304–2309. https://doi.org/10.2514/1.G004347.

[9] Moose, R. L. "An Adaptive State Estimation Solution to the Maneuvering Target Problem." *IEEE Transactions on Automatic Control*, Vol. 20, No. 3, 1975, pp. 359–362. https://doi.org/10.1109/TAC.1975.1100961.

[10] Zhai, G., Wang, Y., and Zhao, Q. "Tracking the Maneuvering Spacecraft Propelled by Swing Propulsion of Constant Magnitude." *Journal of Systems Engineering and Electronics*, Vol. 31, No. 2, 2020, pp. 370–382. https://doi.org/10.23919/JSEE.2020.000014.

[11] Goff, G. M., Black, J. T., and Beck, J. A. "Orbit Estimation of a Continuously Thrusting Spacecraft Using Variable Dimension Filters." *Journal of Guidance, Control, and Dynamics*, Vol. 38, No. 12, 2015, pp. 2407–2420. https://doi.org/10.2514/1.G001091.

[12] Jaunzemis, A. D., Feigh, K. M., Holzinger, M. J., Minotra, D., and Chan, M. W. "Cognitive Systems Engineering Applied to Decision Support in Space Situational Awareness." *Journal of Cognitive Engineering and Decision Making*, Vol. 14, No. 1, 2020, p. 297. https://doi.org/10.1177/1555343419872050.

[13] Ko, H. C., and Scheeres, D. J. "Maneuver Detection with Event Representation Using Thrust Fourier Coefficients." *Journal of Guidance, Control, and Dynamics*, Vol. 39, No. 5, 2016, pp. 1080–1091. https://doi.org/10.2514/1.G001463.

[14] Ko, H. C., and Scheeres, D. J. "Orbit Determination across Unknown Maneuvers Using the Essential Thrust-Fourier-Coefficients." *Acta Astronautica*, Vol. 118, 2016, pp. 90–95. https://doi.org/10.1016/j.actaastro.2015.10.002.

[15] Guang, Z., Xingzi, B., Hanyu, Z., and Bin, L. "Non-Cooperative Maneuvering Spacecraft Tracking via a Variable Structure Estimator." *Aerospace Science and Technology*, Vol. 79, 2018, pp. 352–363. https://doi.org/10.1016/j.ast.2018.05.052.

[16] Visina, R., Bar-Shalom, Y., and Willett, P. "Multiple-Model Estimators for Tracking Sharply Maneuvering Ground Targets." *IEEE Transactions on Aerospace and Electronic Systems*, Vol. 54, No. 3, 2018, pp. 1404–1414. https://doi.org/10.1109/TAES.2018.2793019.

[17] Munir, A., and Atherton, D. P. "Adaptive Interacting Multiple Model Algorithm for Tracking a Manoeuvering Target." *IEE Proceedings: Radar, Sonar and Navigation*, Vol. 142, No. 1, 1995, pp. 11–17. https://doi.org/10.1049/ip-rsn:19951528.

[18] Ruan, Y., and Willett, P. "Multiple Model PMHT and Its Application to the Second Benchmark Radar Tracking Problem." *IEEE Transactions on Aerospace and Electronic Systems*, Vol. 40, No. 4, 2004, pp. 1337–1350. https://doi.org/10.1109/TAES.2004.1386885.

[19] Goff, G. M., Black, J. T., and Beck, J. A. "Tracking Maneuvering Spacecraft with Filter-through Approaches Using Interacting Multiple Models." *Acta Astronautica*, Vol. 114, 2015, pp. 152–163. https://doi.org/10.1016/j.actaastro.2015.05.009.

[20] Singer, R. A. "Estimating Optimal Tracking Filter Performance for Manned Maneuvering Targets." *IEEE Transactions on Aerospace and Electronic Systems*, Vol. AES-6, No. 4, 1970, pp. 473–483. https://doi.org/10.1109/TAES.1970.310128.

[21] Chan, Y. T., Hu, A. G. C., and Plant, J. B. "A Kalman Filter Based Tracking Scheme with Input Estimation." *IEEE Transactions on Aerospace and Electronic Systems*, Vol. AES-15, No. 2, 1979, pp. 237–244. https://doi.org/10.1109/TAES.1979.308710.

[22] Batselier, K., Chen, Z., and Wong, N. "A Tensor Network Kalman Filter with an Application in Recursive MIMO Volterra System Identification." *Automatica*, Vol. 84, 2017, pp. 17–25. https://doi.org/https://doi.org/10.1016/j.automatica.2017.06.019.

[23] Zhu, W., Wang, W., and Yuan, G. "An Improved Interacting Multiple Model Filtering Algorithm Based on the Cubature Kalman Filter for Maneuvering Target Tracking." *Sensors (Switzerland)*, Vol. 16, No. 6, 2016, p. 805. https://doi.org/10.3390/s16060805.

[24] Schiemenz, F., Utzmann, J., and Kayal, H. "Adaptive Gaussian Mixture Based Orbit Determination with Combined Atmospheric Density Uncertainty Consideration." *Advances in Space Research*, Vol. 66, No. 7, 2020, pp. 1609–1634. https://doi.org/https://doi.org/10.1016/j.asr.2020.05.042.

[25] Sung, T. K., and Lee, J. G. "A Modified Input Estimation Technique Using Pseudoresiduals." *IEEE Transactions on Aerospace and Electronic Systems*, Vol. 30, No. 2, 1994, pp. 220–228. https://doi.org/10.1109/7.272280.

[26] Serra, R., Yanez, C., and Frueh, C. "Tracklet-to-Orbit Association for Maneuvering Space Objects Using Optimal Control Theory." *Acta Astronautica*, Vol. 181, 2021, pp. 271–281. https://doi.org/10.1016/j.actaastro.2021.01.026.

[27] Goff, G. M., Showalter, D., Black, J. T., and Beck, J. A. Parameter Requirements for Noncooperative Satellite Maneuver Reconstruction Using Adaptive Filters. No. 38, 2015, pp. 361–374.

[28] Sullivan, J., and D'Amico, S. "Nonlinear Kalman Filtering for Improved Angles-Only Navigation Using Relative Orbital Elements." *Journal of Guidance, Control, and Dynamics*, Vol. 40, No. 9, 2017. https://doi.org/10.2514/1.G002719.

[29] Lubey, D. P., Scheeres, D. J., and Erwin, R. S. "Maneuver Detection and Reconstruction of Stationkeeping Spacecraft at GEO Using the Optimal Control-Based Estimator." *IFAC-PapersOnLine*, Vol. 48, No. 9, 2015, pp. 216–221. https://doi.org/https://doi.org/10.1016/j.ifacol.2015.08.086.

[30] Lemmens, S., and Krag, H. "Two-Line-Elements-Based Maneuver Detection Methods for Satellites in Low Earth Orbit." *Journal of Guidance, Control, and Dynamics*, Vol. 37, No. 3, 2014, pp. 860–868. https://doi.org/10.2514/1.61300.

[31] Holzinger, M. J., Scheeres, D. J., and Alfriend, K. T. "Object Correlation, Maneuver Detection, and Characterization Using Control-Distance Metrics." *Journal of Guidance, Control, and Dynamics*, Vol. 35, No. 4, 2012, pp. 1312–1325. https://doi.org/10.2514/1.53245.

[32] Greaves, J. A., and Scheeres, D. J. "Observation and Maneuver Detection for Cislunar Vehicles." *The Journal of the Astronautical Sciences*, Vol. 68, No. 4, 2021, pp. 826–854. https://doi.org/10.1007/s40295-021-00283-y.

[33] Hall, Z., Singla, P., and Johnson, K. "Reachability-Based Search for Tracking of Noncooperative Maneuvering Satellites in Data Sparse Environment." *The Journal of the Astronautical Sciences*, Vol. 70, No. 2, 2023, p. 9. https://doi.org/10.1007/s40295-023-00365-z.

[34] Hall, Z., and Singla, P. Reachability Analysis Based Tracking: Applications to Non-Cooperative Space Object Tracking. In *Dynamic Data Driven Applications Systems* (F. Darema, E. Blasch, S. Ravela, and A. Aved, eds.), Springer International Publishing, Cham, 2020, pp. 200–207.

[35] Jain, A., and Singla, P. Stochastic Reachability Analysis Using Sparse-Collocation Method. In *AIAA SCITECH 2023 Forum*, American Institute of Aeronautics and Astronautics, 2023.

[36] Hall, Z., and Singla, P. "Higher-Order Sensitivity Matrix Method for Probabilistic Solution to Uncertain Lambert Problem and Reachability Set Problem." *Celestial Mechanics and Dynamical Astronomy*, Vol. 132, No. 10, 2020, p. 50. https://doi.org/10.1007/s10569-020-09988-y.

[37] Hall, Z., Schwab, D., Eapen, R., and Singla, P. Reachability-Based Approach for Search and Detection of Maneuvering Cislunar Objects. In *AIAA SCITECH 2022 Forum*, American Institute of Aeronautics and Astronautics, 2021.

[38] Park, R. S., and Scheeres, D. J. "Nonlinear Mapping of Gaussian Statistics: Theory and Applications to Spacecraft Trajectory Design." *Journal of Guidance, Control, and Dynamics*, Vol. 29, No. 6, 2006, pp. 1367–1375. https://doi.org/10.2514/1.20177.

[39] Park, R. S., and Scheeres, D. J. "Nonlinear Semi-Analytic Methods for Trajectory Estimation." *Journal of Guidance, Control, and Dynamics*, Vol. 30, No. 6, 2007, pp. 1668–1676. https://doi.org/10.2514/1.29106.

[40] Boone, S., and McMahon, J. "Orbital Guidance Using Higher-Order State Transition Tensors." *Journal of Guidance, Control, and Dynamics*, Vol. 44, No. 3, 2021, pp. 493–504. https://doi.org/10.2514/1.G005493.

[41] Boone, S., and McMahon, J. "Variable Time-of-Flight Spacecraft Maneuver Targeting Using State Transition Tensors." *Journal of Guidance, Control, and Dynamics*, Vol. 44, No. 11, 2021, pp. 2072–2080. https://doi.org/10.2514/1.G005890.

[42] Yang, Z., Luo, Y., Lappas, V., and Tsourdos, A. "Nonlinear Analytical Uncertainty Propagation for Relative Motion near J2-Perturbed Elliptic Orbits." *Journal of Guidance, Control, and Dynamics*, Vol. 41, No. 4, 2018, pp. 888–903. https://doi.org/10.2514/1.G003071.

[43] Yang, Z., Luo, Y., and Zhang, J. "Nonlinear Semi-Analytical Uncertainty Propagation of Trajectory under Impulsive Maneuvers." *Astrodynamics*, Vol. 3, No. 1, 2019, pp. 61–77. https://doi.org/10.1007/s42064-018-0036-7.

[44] Luo, Y., and Yang, Z. "A Review of Uncertainty Propagation in Orbital Mechanics." *Progress in Aerospace Sciences*, Vol. 89, 2017, pp. 23–39. https://doi.org/10.1016/j.paerosci.2016.12.002.

[45] Turner, J. D. "Automated Generation of High-Order Partial Derivative Models." *AIAA Journal*, Vol. 41, No. 8, 2003, pp. 1590–1598. https://doi.org/10.2514/2.2112.

[46] Hu, Y., Sharf, I., and Chen, L. "Three-Spacecraft Autonomous Orbit Determination and Observability Analysis with Inertial Angles-Only Measurements." *Acta Astronautica*, Vol. 170, 2020, pp. 106–121. https://doi.org/10.1016/j.actaastro.2020.01.005.

[47] Hu, Y., Sharf, I., and Chen, L. "Distributed Orbit Determination and Observability Analysis for Satellite Constellations with Angles-Only Measurements." *Automatica*, Vol. 129, 2021, p. 109626. https://doi.org/10.1016/j.automatica.2021.109626.

[48] Kelecy, T., and Jah, M. "Detection and Orbit Determination of a Satellite Executing Low Thrust Maneuvers." *Acta Astronautica*, Vol. 66, No. 5, 2010, pp. 798–809. https://doi.org/https://doi.org/10.1016/j.actaastro.2009.08.029.

[49] Mook, D. J., and Junkins, J. L. "Minimum Model Error Estimation for Poorly Modeled Dynamic Systems." *Journal of Guidance, Control, and Dynamics*, Vol. 11, No. 3, 1988, pp. 256–261. https://doi.org/10.2514/3.20302.